Response to Reviewers

Manuscript Title:
"Differential Column Measurements Using Compact Solar-Tracking Spectrometers"

We would like to thank the reviewers for carefully reading the paper and giving helpful comments.

Below, the reviewers' original text is included in typewriter font. The answers are highlighted in blue, sans-serif fonts. After our responses to the reviewers, we have listed the addtional changes we have made to the manuscript.

Reviewer 1

General Comments:

In section 2 there is too little description of the basic solar FTS measurement – the reader is assumed to be familiar with solar FTS remote sensing and previous work. A summary of the measurement technique, referring back to TCCON and the previous papers on this instrument, would be useful for all readers, as it is it is directed only to those who are already involved in these measurements.

Thanks for this comment. We added one subsection (Sec. 2.1), providing background information about the solar-tracking FTS techniques and discussing existing networks. We added citations to NDACC (Hannigan (2011)), and to TCCON (Toon et al. (2009), Wunch et al. (2010), Wunch et al. (2011)). For EM27/SUN, Gisi et al. (2011), Gisi et al. (2012), Frey et al. (2015), Hase et al. (2015), Klappenbach et al. (2015), Hedelius et al. (2016) are cited. For the working principles of FTS, Davis et al. (2001) and Griffiths and De Haseth (2007) are referred. The added section please find on page 3 of the manuscript.

Section 3 is about precision and accuracy of the technique, but the authors use the term "precision" and other terms in incorrect ways. I recommend a reading of the IUPAC publication commonly known as GUM: "Evaluation of measurement data Guide to the expression of uncertainty in measurement" by the Joint Committee for Guides in Metrology, JCGM 100-2008 (available from the BIPM website). "Precision" is a general term, which is not defined for quantitative uncertainty assessment – quantities such as repeatability and reproducibility have specific, quantitative meanings and should be used in quantitative assessments of random uncertainty. Similarly there are more specific terms for "accuracy". In particular, in most cases in this paper, "precision" is used very loosely and mostly means "repeatability". Since the focus of section 2 is quantification of uncertainty, I recommend using correct terminology.

Thank you very much for this comment and providing the references. We looked at "JCGM 200:2008 International vocabulary of metrology Basic and general concepts and associated terms (VIM)", which defines "measurement precision" as the closeness of agreement between indications or measured quantity values obtained by replicate measurements on the same or similar objects under specified conditions, and explicitly says that "Measurement precision is used to define measurement repeatability, intermediate measurement precision, and measurement reproducibility."

In the Wikipedia article Accuracy and precision, "precision" is described as: "The precision of a measurement system, related to reproducibility and repeatability, is the degree to which repeated measurements under unchanged conditions show the same results". According to ISO 5725-1, "precision" is the closeness of agreement among a set of results.

Therefore, we would like to keep the terminology "precision", which is also used in the field of laser spectroscopy for quantifying the measurement repeatability.

The authors use "gradient" throughout when they really mean "difference". A gradient is difference per unit length, eg 2 ppm km-1, not 2 ppm as used here. I found this confusing when reading, and recommend that all instances of "gradient" be sought out and replaced with "difference" where appropriate.

Thank you for pointing out this problem. We fully agree and changed the document accordingly. Note, that there are some occurrences of "gradient" in the document, where we actually mean difference per unit length, and thus kept the expression.

Units: please quote units correctly, eg m s-1 not m/s, molec m-2 s-1, not molec/(m2s) as in Table 1. See the IUPAC "green book" (Cohen, et al. (2007)). Quantities, Units and Symbols in Physical Chemistry. Cambridge, IUPAC, RSC Publishing) for authority on units.

We changed the units written as the product of units, without any multiplication sign and left one space between the unit symbols.

Use of "%" and "‰"- I found it very confusing to mix these two quantities, it is too easy not to notice "‰" and read it as %. I recommend using % throughout.

Thanks for this note, we changed all the "‰" to "%".

Specific and technical comments:

Section 3.1. It is acceptable to use "precision" when speaking generally, but in cases when a value is assigned to an uncertainty, "precision" should be replaced by the appropriate specific quantity "repeatability" or "reproducibility". There are many instances, please search and replace P4 L10: "underestimate the true precision" really means repeatability and is ambiguous since high precision is a small number. Perhaps replace with "overestimate the true random uncertainty of the measurement."

Thank you very much for this comment. As for our answer to the use of "precision", please see our reply to your general comment.
We changed "underestimate the true precision" to "overestimate the true random uncertainty of the measurement."

P4 L21: Allan Deviation, not standard deviation.
P4 L28: "Allan standard deviation" is incorrect - replace with "Allan deviation", which is the square root of the Allan Variance; they are not calculated in the same way as variance and standard deviation and should not be confused. There are many examples of "Allan standard deviation" throughout which should be replaced by "Allan deviation" = please search and replace (including figures, eg axis labels in Fig 1).

Thank you for pointing this out. We replaced "Allan standard deviation" with "Allan deviation" throughout the document.

P5 L11 "System Robustness" "Robust" has a specific meaning in statistics, and since this is a statistical section, I would recommend System stability as a better title.

We changed "robustness" to "stability", thanks!

P11 L12: "Column gradient observations" - first of many examples where "difference" or "differential" should replace "gradient"

We changed "column gradient observations" to "differential column observations".

P6 L5: Here "precision" is used when "accuracy" is meant - this sentence describes a systematic error.

Thanks. The previous sentence was misleading, we changed the sentence to "Retrievals for ha have been scaled with RG for the Allan analysis (Sec. 3.1) "

P7 L23: The usual Reynolds notation is to use u' for the turbulent wind speed component, rather than uturb, so that u(t) = u(bar) + u'(t)

Thanks for pointing this out. We would prefer to use u_{turb}, because u'(t) could be mis-understood as the first derivative of the signal u(t). Hence, u_{turb} might be less prone to misunderstanding, especially, for readers from other disciplines.

P10 L19: Please explain the transient peak around solar noon – what is it due to, and justification for its removal.

We added section 4.3.2 "Transient Peak at Chino" to discuss the possible cause of the transient peak. The transient peaks are removed for calculating the column difference, since they are not associated with the local dairy farms.

P11 L14: The meaning of this heading is quite unclear. I suggest replacing "gradient" with "difference" as commented earlier, and bring the second paragraph beginning Pasadena ..." ahead of the first, so it comes first after the heading. Most of the confusion lies in the incorrect use of "gradient".

Thanks! We changed the title, and changed "gradient" to "difference". Also we changed the order of the first two paragraphs and hopefully the content is more clear now.

P12 Fig 4: The lowest panel would be very much improved if both the XCO2 and XCH4 axis had a common zero line.

Thanks much for this suggestion! Now the two y-axis share a common zero line in Fig. 4.

P12 Fig 5: In the plot, cut off the negative axes at (-1,-5) to better utilize the space and avoid large empty area of the plot. Use the (0,0) axes rather than L and right axes, so the origin is clear.

Thanks. We cut off the negative axes, and we use "+" to illustrate (0,0).

P13 Fig 6: Same comment as Fig 5. The origin crosses cant be seen. The time periods are quite unclear – what are [-1 h : 0 h] etc, relative to what time? More detail in caption required.

Thank you for the question and the suggestion. We changed the caption as "Left figure shows the time period between 1 hour before solar noon and 2 hours after solar noon, and right plot shows the time period 2 to 4 hours after solar soon."

P13 L1: please rephrase as " a lower DXCH4/DXCO2 ratio" since this is the way the plots are presented (with CH4 on the Y axis).

Done.

Appendix D: The plots of the O2 column are not particularly informative, since they reflect mostly pressure not spectroscopic retrieval. I suggest to replace these plots with the O2 column : pressure ratio (corrected to dry air) – this should be a constant with a known value related to 0.2095 mole fraction of O2 in air.

Thanks for this suggestion. Here the O_2 column are shown for determining column dry air and its uncertainty. We added one paragraph in Appendix D to clarify the purpose:
"According to Fig. 11, the oxygen column number density over the dairy area is $4.493 \cdot 10^{28}$ molec. m$^{-2} \pm 0.5\%$, which is used to calculate column$_{\text{dryair}}$, the column number density of dry air. column$_{\text{dryair}}$ is needed in the column model (Eq. 2) for the emission estimates. The uncertainty is mainly associated with the differences in altitudes between sites."

Reviewer 2

In Fig. 2 results of different days of observation are presented. To compare results obtained
with different retrieval codes the same days should be presented for both cases. Side by side
measurements were conducted over many months, but just a few days are presented in this paper.

Thank you for this comment. Now the same days are presented for GFIT and PROFFIT to infer the mean calibration factors: three days in Boston and five days in Pasadena.

The side-by-side measurements are conducted since August 2014. For clarity reasons, we chose 8 days for deriving the calibration factors that are used for the field study.

The modified figures please find on page 7 of the manuscript.

In the time series of the upwind site a transient peak is observed (Fig. 3). When the up- and
downwind sites are located along the trajectory a downwind peak should be present as well?
Such peaks travelling from up- to downwind site may provide a proof of sampling the same air
mass.

We thank the reviewer for the very useful hint. Yes, we think the transient peaks are also observable at the downwind site, but much weaker probably due to dispersion. More discussions are added in section 4.3.2.

Table 3 lists the calibration factors for the spectrometers. I recommend to include these
factors for side by side measurements performed before and after the campaign. In order to
show the stability of the instruments these factors obtained before and after the campaign
should be discussed and compared with those presented by Frey et al., 2015.

Thanks for this comment. We add Table 1 to the paper and list the calibration factors before and during the campaign. After the transport after the campaign, one screw for the flipping mirror was loose for ha and we opened the instrument to fix it, which might have changed the instrument behavior and resulted in a slightly different calibration factor. Since it is a technical problem, not representative for the overall behavior of EM27/SUN and differential column measurements, we decided to not report the calibration factors after the campaign in the paper.

The added table please find below:

	$\overline{R_{\mathrm{CH_4}}}$		$\overline{R_{\mathrm{CO_2}}}$	
	GFIT	PROFFIT	GFIT	PROFFIT
Before	0.99574	0.99813	0.99877	0.99838
During	0.99580	0.99809	0.99881	0.99834
Both	0.99578	0.99810	0.99880	0.99835

Table 1: Calibration factors $\overline{R_G}$ for $X_{\mathrm{CH_4}}$ and $X_{\mathrm{CO_2}}$ before and during the field campaign, determined by forcing linear regression line go through zero. $\overline{R_G}$, determined using all data, are provided in the last row and used for the field study.

Additional Changes

1. We rephrased the first sentence in the introduction.

2. We changed the term "scaling factor" to "calibration factor".

3. We added a sentence "5 minutes averaged wind information from Automated Surface Observing System (ASOS) is used." in Sec. 4.1 to indicate where the wind data are coming from.

4. We expand Table 2 with Peischl's number for an easy reading and comparing.

5. We modified the title of Appendix C as "Retrieval Sensitivity to Pressure Inputs"

6. We changed the title of Appendix E to "Validation of Wind Model", and added Appendix E2 for validation with HSPLIT simulations, and added acknowlegment for HYSPILT,

7. We changed the order of Appendix E and Appendix F.

8. We thank the reviewers for helpful comments.

9. In some sentences the grammar was off, we corrected them.

References

Davis, S. P., Abrams, M. C., and Brault, J. W.: Fourier transform spectrometry, Academic Press, 2001.

Frey, M., Hase, F., Blumenstock, T., Groß, J., Kiel, M., Mengistu Tsidu, G., Schäfer, K., Sha, M., and Orphal, J.: Calibration and instrumental line shape characterization of a set of portable FTIR spectrometers for detecting greenhouse gas emissions, Atmospheric Measurement Techniques, 8, 3047–3057, 2015.

Gisi, M., Hase, F., Dohe, S., and Blumenstock, T.: Camtracker: a new camera controlled high precision solar tracker system for FTIR-spectrometers, Atmospheric Measurement Techniques, 4, 47–54, doi:10.5194/amt-4-47-2011, 2011.

Gisi, M., Hase, F., Dohe, S., Blumenstock, T., Simon, A., and Keens, A.: XCO_2-measurements with a tabletop FTS using solar absorption spectroscopy, Atmospheric Measurement Techniques, 5, 2969–2980, 2012.

Griffiths, P. R. and De Haseth, J. A.: Fourier transform infrared spectrometry, vol. 171, John Wiley & Sons, 2007.

Hannigan, J. W.: NDACC IRWG: Evolution of Ground-Based Global Trace Gas Infrared Remote Sensing, in: Fourier Transform Spectroscopy, p. FMC1, Optical Society of America, 2011.

Hase, F., Frey, M., Blumenstock, T., Groß, J., Kiel, M., Kohlhepp, R., Mengistu Tsidu, G., Schäfer, K., Sha, M., and Orphal, J.: Application of portable FTIR spectrometers for detecting greenhouse gas emissions of the major city Berlin, Atmospheric Measurement Techniques, 8, 3059–3068, 2015.

Hedelius, J. K., Viatte, C., Wunch, D., C., R., Toon, G. C., Chen, J., Jones, T., Wofsy, S. C., Franklin, J. E., Parker, H., Dubey, M., and Wennberg, P. O.: Assessment of errors and biases in Xgas retrieved from a low resolution spectrometer (EM27/SUN), Atmospheric Measurement Techniques Discussion, doi:10.5194/amt-2016-39, in review, 2016.

Klappenbach, F., Bertleff, M., Kostinek, J., Hase, F., Blumenstock, T., Agusti-Panareda, A., Razinger, M., and Butz, A.: Accurate mobile remote sensing of XCO 2 and XCH 4 latitudinal transects from aboard a research vessel, Atmospheric Measurement Techniques, 8, 5023–5038, 2015.

Toon, G., Blavier, J.-F., Washenfelder, R., Wunch, D., Keppel-Aleks, G., Wennberg, P., Connor, B., Sherlock, V., Griffith, D., Deutscher, N., et al.: Total column carbon observing network (TCCON), in: Fourier Transform Spectroscopy, p. JMA3, Optical Society of America, 2009.

Wunch, D., Toon, G. C., Wennberg, P. O., Wofsy, S. C., Stephens, B. B., Fischer, M. L., Uchino, O., Abshire, J. B., Bernath, P., Biraud, S. C., et al.: Calibration of the Total Carbon Column Observing Network using aircraft profile data, Atmospheric Measurement Techniques, 3, 1351–1362, 2010.

Wunch, D., Toon, G. C., Blavier, J. F., Washenfelder, R. A., Notholt, J., Connor, B. J., Griffith, D. W., Sherlock, V., and Wennberg, P. O.: The total carbon column observing network, Philos Trans A Math Phys Eng Sci, 369, 2087–112, 2011.

Differential Column Measurements Using Compact Solar-Tracking Spectrometers

Jia Chen[1,4], Camille Viatte[2], Jacob K. Hedelius[2], Taylor Jones[1], Jonathan E. Franklin[1], Harrison Parker[3], Elaine W. Gottlieb[1], Paul O. Wennberg[2], Manvendra K. Dubey[3], and Steven C. Wofsy[1]

[1]School of Engineering and Applied Sciences and Department of Earth and Planetary Sciences, Harvard University, Cambridge, MA 02138, USA
[2]Division of Geological and Planetary Sciences, California Institute of Technology, Pasadena, CA 91125, USA
[3]Earth and Environmental Sciences, Los Alamos National Laboratory, Los Alamos, NM 87545, USA
[4]now at Electrical and Computer Engineering, Technische Universität München, Munich, 80333, Germany

Correspondence to: Jia Chen (jia.chen@tum.de)

Abstract. We demonstrate the use of compact solar-tracking Fourier transform spectrometers (Bruker EM27/SUN) for differential measurements of the column-averaged dry-air mole fractions of CH_4 and CO_2 within urban areas. Using Allan variance analysis, we show that the differential column measurement has a precision of ~~0.1‰~~ 0.01% for X_{CO_2} and X_{CH_4} using an optimum integration time of 10 min, ~~which corresponds to standard~~ corresponding to Allan deviations of 0.04 ppm, and 0.2 ppb, respectively. The sensor system is very stable over time and after relocation across the continent. We report tests of the differential column measurement, and its sensitivity to emission sources, by measuring the ~~downwind minus upwind column gradient~~ downwind-minus-upwind column difference ΔX_{CH_4} across dairy farms in the Chino California area and using the data to verify emissions reported in the literature. ~~Spatial column gradient ratios~~ Ratios of spatial column differences $\Delta X_{CH_4}/\Delta X_{CO_2}$ were observed across Pasadena within the Los Angeles basin, indicating values consistent with regional emission ratios from the literature. Our precise, rapid measurements allow us to determine significant short-term variations (5-10 minutes) of X_{CO_2} and X_{CH_4}, and to show that they represent atmospheric phenomena.

Overall, this study helps establish a range of new applications for compact solar-viewing Fourier transform spectrometers. By accurately measuring the small differences in integrated column amounts across local and regional sources, we directly observe the mass loading of the atmosphere due to the influence of emissions in the intervening locale. The inference of the source strength is much more direct than inversion modeling using only surface concentrations, and less subject to errors associated with small-scale transport phenomena.

1 Introduction

Cities and their surrounding urban regions occupy less than 3% of the global land surface (Grimm et al. (2008)), but are home to 54% of the world population (WHO (2014)) and account for ~~∼~~ more than 70% ~~(UNHabitat (2011)) of total fossil fuel emissions~~ of global fossil-fuel CO_2 emissions (Gurney et al. (2015)). Hence, accurate methods for measuring urban and regional scale carbon fluxes are required in order to design and implement policies for emissions reduction initiatives.

It is challenging to use *in situ* measurements of CO_2 and CH_4 to derive emission fluxes in urban regions. Surface concentrations typically have high variance due to the influence of nearby sources, and they are strongly modulated by mesoscale transport phenomena that are difficult to simulate in atmospheric models. These include the variation of the depth of the planetary boundary layer (PBL), sea breeze, and topographic flows, etc. (McKain et al. (2012); Bréon et al. (2015)).

5   The mass loading of the atmosphere can be directly determined by measuring the column integrated amount of a tracer through the whole atmosphere. Column measurements are insensitive to vertical redistribution of tracer mass, e.g. due to growth of the PBL, and are also less influenced by nearby point sources whose emissions are concentrated in a thin layer near the surface. Column observations are more compatible with the scale of atmospheric models and hence provide stronger constraints for inverse modeling (Lindenmaier et al. (2014)).

10   One potential drawback, however, is that column observations are sensitive to surface emissions over a very wide range of spatial scales, spanning nearby emissions and all those upwind in the urban, continental, and hemispheric domains. In this paper we demonstrate how to use simultaneous measurements of the column-averaged dry-air mole fractions (DMFs) of CH_4 and CO_2 (denoted by X_{CH_4} and X_{CO_2}, respectively) at upwind and downwind sites to mitigate this limitation. The horizontal gradients *within* a region are relatively insensitive to surface fluxes upwind of the domain, providing favorable input for regional

15 flux inversions.

     We use three matched, compact Fourier Transform spectrometers to measure the small (~~1‰~~0.1%) differences of X_{CH_4} and X_{CO_2}, and we demonstrate sufficient precision and speed to determine emission rates at the urban scale. By directly measuring spatial and temporal gradients of the mass loading, we reduce the sensitivity of inverse model results to atmospheric fine structure, such as may arise from vertical redistribution of trace gases, and that often complicates interpretation of surface *in*

20 *situ* data (Chang et al. (2014)).

     Our ground-based network of spectrometers measuring gradients of column amounts could enable new approaches to validate the *urban-rural gradients* of satellite observations such as OCO-2 (Crisp et al. (2008); Frankenberg et al. (2015)) and TROPOMI (Veefkind et al. (2012)). In contrast to the large, high spectral resolution instruments of the Total Carbon Column Observing Network (TCCON), which are not easily re-located, the compact spectrometers can be deployed directly under

25 satellite tracks that pass near major cities, to assess potential artifacts in satellite-derived tracer gradients that might arise from urban or rural differences in aerosol burden, land surface properties, etc.

     Several recent papers have studied column-averaged concentrations of trace gases to derive source fluxes. Wunch et al. (2009) observed diurnal patterns for X_{CO_2}, X_{CH_4}, and X_{CO} over Los Angeles, similar to the model simulations of McKain et al. (2012) for Salt Lake City. Kort et al. (2012) used GoSAT satellite data to measure the difference between CO_2 columns

30 inside and outside Los Angeles, and to derive a top-down inventory for CO_2. Papers by Stremme et al. (2009, 2013) and Té et al. (2012) used total column measurements from a ground-based Fourier transform spectrometer (FTS) to estimate and monitor CO emission in Mexico City and Paris, respectively. Mellqvist et al. (2010) studied plumes from industrial complexes, and Lindenmaier et al. (2014) examined plumes from two power plants and discriminated them. Kort et al. (2014) quantified large methane sources missing in inventories at Four Corners, NM. However, these studies did not have simultaneous upwind

35 and downwind column data, one of the novel elements of the present paper.

Frey et al. (2015) and Hase et al. (2015) reported deployments of multiple FTSs of the same type as employed here, deriving calibration and stability characteristics in a field setting. We extend this analysis by determining the Allan variances of column concentration *differences* between spectrometer pairs deployed side-by-side, providing a rigorous assessment of the precision of the differential column measurements.

Here we study local scale gradients in X_{CO_2} and X_{CH_4} in two applications. First, we deployed our spectrometers upwind and downwind of the dairy farms in Chino, California (about 50 km^2 area), and use the data to compare with emissions reported in the literature. A second application uses the observed ratio of differences in X_{CO_2} and X_{CH_4}, i.e. $\Delta X_{CH_4}/\Delta X_{CO_2}$, to characterize emission ratios for these gases within the Los Angeles basin.

In another application of the compact spectrometers, we co-located spectrometers to demonstrate measurement of short-term (5-10 minutes) variations of column-averaged DMFs in the atmosphere. The high precision measurements with rapid scan rates are an advantage of the compact spectrometers compared to larger, higher spectral resolution spectrometers. We show that high frequency observations can be used to quantify the influence of sporadic events, such as plumes within the PBL or instabilities across the top of the mixed layer (ML), on measurements in urban areas.

2   Differential Column Network

2.1   [Column Measurement and Existing FTS Network]

Solar-tracking FTSs can be used to measure the gas column number densities, i.e. the number of gas molecules per unit area in the atmospheric column (column$_G$, unit: molec. m^{-2}). The sun is used as light source and the FTS is located on the ground for measuring the solar radiation transmitted through the atmosphere. The recorded sun radiation spectrum is broadband and covers the absorption fingerprints of diverse gas species including CO_2, CH_4, H_2O and O_2. The attenuation of the solar intensity at specific frequencies provides a measure for the column number density for various gases. For further details of the modeling of the atmsopheric transmittance spectrum, please see Wunch et al. (2011) and Hase et al. (2004), for the working principles of FTS please refer to Davis et al. (2001), and Griffiths and De Haseth (2007).

The existing FTS networks include NDACC (Hannigan (2011)), i.e. "Network for the Detection of Atmospheric Composition Change", and TCCON (Toon et al. (2009), Wunch et al. (2010), Wunch et al. (2011)). NDACC measures at mid-infrared wavelengths and detects atmospheric O_3, HNO_3, HCl, HF, CO, N_2O, CH_4, HCN, C_2H_6, and $ClONO_2$, chosen to help understand the physical and chemical state of the upper troposphere and the stratosphere. The TCCON network focuses on column measurements of greenhouse gases, mainly CO_2, CH_4, N_2O and CO, at near-infrared wavelengths. It uses the Bruker IFS 125HR spectrometer that is large in dimension (room size) and heavyweight (>500 kg, Bruker (2006)). The spectra in the TCCON network are recorded with a spectral resolution of approx. 0.02 cm^{-1} and require about 170 s for one forward/backward scan pair (Hedelius et al. (2016)).

2.2 Differential Column Measurement with Compact FTS

Our differential column network uses at least two spectrometers to make simultaneous measurements of column number densities of CO_2, CH_4, and O_2. We then compute the column-averaged DMFs for each gas G, i.e., $X_G = \text{column}_G / \text{column}_{O_2} \cdot 0.2095$ (Wunch et al. (2011)) ~~and gradients for a gas G~~, and differences, i.e., $\Delta X_G = X_G^d - X_G^u$, where X_G^d and X_G^u stand for column-averaged DMFs at downwind and upwind sites.

Our sensors are two EM27/SUN FTS units owned by Harvard University, and one owned by Los Alamos National Laboratory, #45, 46, and 34 Bruker Optics (designated *ha*, *hb*, and *pl*, respectively). They are compact (62.5 cm × 35.6 cm × 47.3 cm) and light-weight (22.8 kg including the sun tracker), with spectral resolution of 0.5 cm^{-1} and a ~~forward/backward~~ scan time of 5.8 s (forward or backward scan). The EM27/SUN tracks the sun precisely (1 σ: 11 arc s) using a camera for fine alignment of the tracking mirrors (Gisi et al. (2011)). It is mechanically very robust, with excellent precision in retrieving X_{CO_2} and X_{CH_4} (Gisi et al. (2012), Klappenbach et al. (2015), Hedelius et al. (2016)), comparable to Bruker IFS 125HR used in the TCCON network Wunch et al. (2011).

We carried out extensive side-by-side measurements of *ha* and *hb* in Boston and Pasadena, over many months, thoroughly examining precision and robustness, and also compared these systems to the TCCON spectrometer in Pasadena, California (Hedelius et al. (2016)). We confirm that these spectrometers are ~~extraordinarily~~ stable (Frey et al. (2015)). We show that comparing pairs of them cancels out most of the systematic error and bias from diverse sources, e.g. spectroscopic and retrieval errors, instrument bias, and errors in pressure and temperature, enabling us to determine ~~1‰~~ 0.1% differences in column-averaged DMFs across the network.

3 System Characterization

3.1 ~~Assessing~~ Allan Analysis for System Precision

Known standards cannot be exchanged for the ambient air in a total column measurement, hence it is difficult to assess the precision of atmospheric measurements end-to-end. Two commonly used literature methods for precision estimates have been based on:

1. *Measurements of the standard deviation of the DMF time series, with the trend removed subtracting a moving average (Gisi et al. (2012)).* This approach is confounded by real variations in the atmosphere that occur on short time scales (*vide infra*).

2. *The residual of the spectral fit.* This estimate does not separate systematic errors, e.g. errors in spectroscopic database and modeling of instrument line shape, from the measurement noise, and therefore may ~~underestimate the true precision~~ overestimate the true random uncertainty of the measurement (*cf.* Fu et al. (2014)).

In this paper we use the Allan variance method (Allan (1966), Werle et al. (1993)) to estimate the measurement precision. Fig. 1 shows the Allan ~~standard~~ deviations of the *differences* in column-averaged DMFs measured simultaneously by *ha* and

hb at the same location, i.e, $\Delta X_G(t) = X_G^{hb}(t) - X_G^{ha}(t)$. The Allan variance of ΔX_G is denoted by $\sigma^2_{allan,\Delta X_G}$, which is the expectation value $\langle \rangle$ of the difference between adjacent samples averaged over the time period τ:

$$\sigma^2_{allan,\Delta X_G}(\tau) = \frac{1}{2} \left\langle (\overline{\Delta X_{G,n+1}} - \overline{\Delta X_{G,n}})^2 \right\rangle, \tag{1}$$

with $\overline{\Delta X_{G,n}} = \frac{1}{\tau} \int_{t_n}^{t_n+\tau} \Delta X_G(t) dt$. Practically $\overline{\Delta X_{G,n}}$ is the mean of all ΔX_G measurements within the time interval $[t_n, t_n + \tau)$.

According to the Allan variance plots:

– The optimal integration time, given by the minimum in the Allan standard deviation, is 10 to 20 min, for both X_{CO_2} and X_{CH_4}.

– When averaging 10 min, the precision (1 standard deviation) of the EM27/SUN differential column measurement is 0.04-0.05 ppm (~~0.1‰~~0.01%) for X_{CO_2} and 0.1-0.2 ppb (~~0.1‰~~0.01%) for X_{CH_4}. Since the two instruments are statistically uncorrelated, the individual measurement noise is smaller by factor $1/\sqrt{2}$, indicating precision comparable to near infrared *in situ* laser spectrometers with commensurate optical path length and integration time (Picarro (2015a, b)). Note that these precision estimates represent the full end-to-end processing of the observations, including deriving the spectrum from the interferogram, retrieving the column number densities in the atmosphere, and normalizing with the O_2 column amount to obtain the column-averaged DMFs.

– When integrating less than 10 min, the Allan ~~standard~~ deviation follows a slope of -1/2 in the double logarithmic scale, indicating white noise ($\tau^{-1/2} \to f^0$), which has a constant power spectral density over the frequency f. As the averaging time τ increases beyond 10 min, the Allan ~~standard~~ deviation rises a little, showing a small color noise component ($\tau^{1/2} \to f^{-2}$), which arises from instrument drift, in part due to temperature differences inside of the spectrometers. There is also a small divergence between the measurements of ha and hb at high solar zenith angles, traceable to their slightly different instrument line shapes (ILSs). The measured ILS parameters are given in Appendix A. Microscale eddies have durations of 10 s to 10 min and length scales from tens to hundreds of meters (Stull (1988), Fig. 2.2). Therefore atmospheric turbulence probably does not play a major role in the Allan plot because there is little color noise within time scale ≤ 10 min for two spectrometers looking along atmospheric paths separated by only a few meters.

We use a shorter integration time (5 min) for measuring emissions from local and regional scale sources (Sec. 4.1 and 4.2), in order to retain high frequency atmospheric signals, giving us precision of 0.05-0.06 ppm for ΔX_{CO_2} and 0.2-0.3 ppb for ΔX_{CH_4} (see Fig. 1). To study the short-term variations due to pollution plumes or turbulent eddies we use 2 min integration time (Sec. 4.3).

3.2 System ~~Robustness~~Stability

~~Column gradient~~ Differential column observations by two spectrometers will inevitably have bias in addition to fluctuations and drift. For the EM27/SUN, small differences in the alignments of the interferometers result in minute, but observable and systematic, deviations in the retrieval results. We examined the biases between ha and hb over a long period of time to
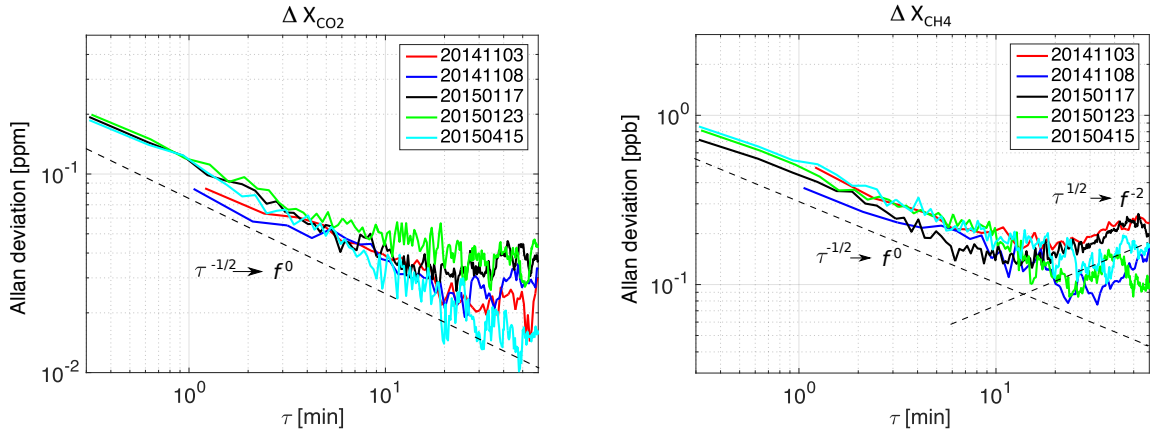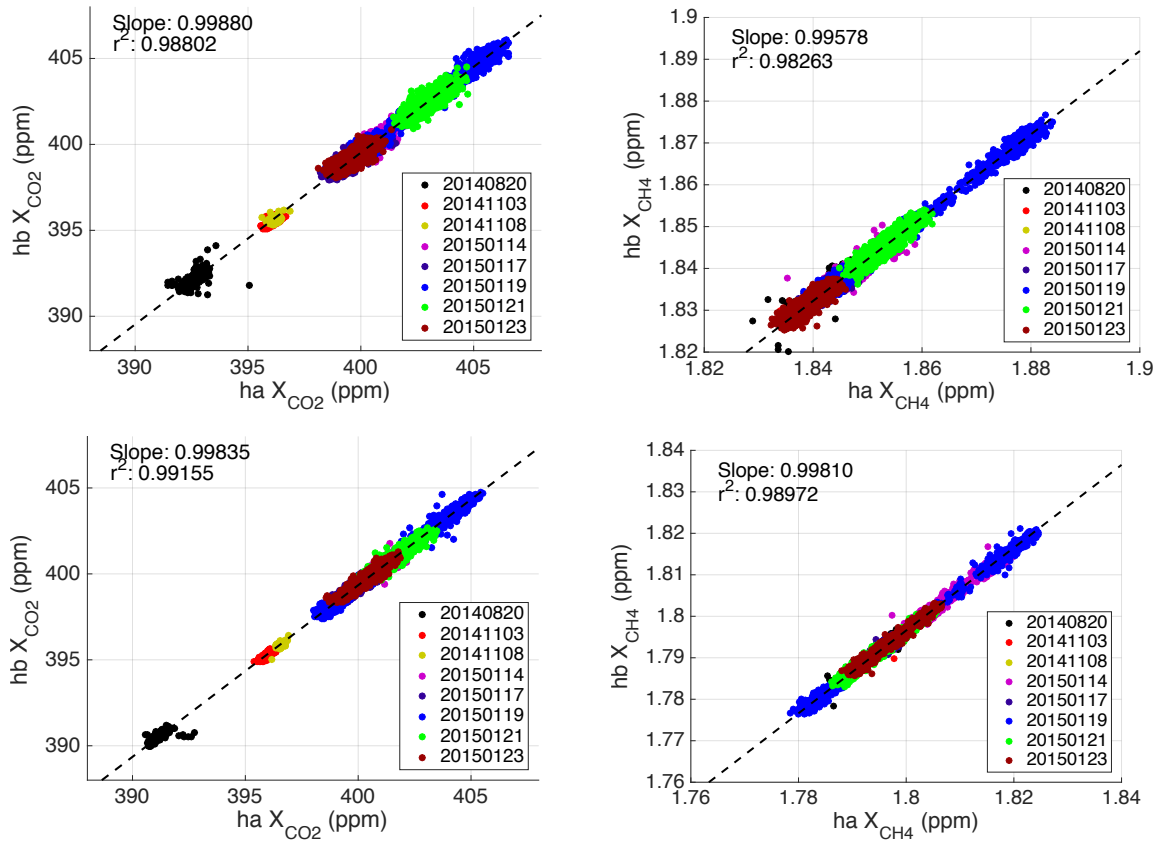
Figure 1. Allan ~~standard~~ deviation $\sigma_{allan,\Delta X_{CO2}}$ and $\sigma_{allan,\Delta X_{CH4}}$ as a function of the integrating time τ. The black dashed lines represent a slope of $-1/2$ and a slope of $1/2$, which correspond to power spectral densities $S(f) = f^0$ (white noise) and $S(f) = f^{-2}$ (Brownian noise), respectively. The Allan ~~standard~~ deviation follows a slope of $-1/2$ up to an integration time of 10 to 20 min, and then stays constant ($S(f) = f^{-1}$), and subsequently turns over to a slope of $1/2$, which describes a linear drift.

determine if these errors can be effectively corrected by applying a constant ~~scaling~~ calibration factor to the retrieval of one instrument to match the performance of the other. The ~~scaling~~ calibration factors are determined assuming a linear model, i.e. $X_G^{hb} = X_G^{ha} \cdot \overline{R_G}$, and for each gas individually.

The value of $\overline{R_G}$ was ~~very~~ consistent over time for the two Harvard EM27/SUNs, including shipment across the ~~continent~~
5 ~~and back~~ contiguous United States (Fig. 2, Table 1). We used two retrieval software systems, ~~GFIT~~ I2S (~~Wunch et al. (2015))~~ interferogram-to-spectrum) combined with GFIT nonlinear least-squares spectral fitting retrieval software (Wunch et al. (2015), Hedelius et al. (2016)), and PROFFIT (Hase et al. (2004)). ~~$\overline{R_G}$ is 0.99880 for X_{CO_2} with GFIT, 0.99835 with PROFFIT; 0.99577 for X_{CH_4} with GFIT, 0.99814 with PROFFIT. Even though the scaling~~ The calibration factors are slightly different for GFIT and PROFFIT, traceable to their specific modeling of the ILS, various priors for the volume mixing ratio profiles, and
10 unequal spectral microwindows that are used. Nevertheless, $\overline{R_G}$ is consistent ~~for different days using one retrieval software~~ in Boston and Pasadena, before and during the campaign, when the same retrieval settings are used. Retrievals for ha have been scaled with $\overline{R_G}$ for the ~~precision assessment above~~ Allan analysis (Sec. 3.1) and for the scientific applications (Sec. 4) below. ~~Scaling~~ Calibration factors for pl are shown in ~~Tab. 4~~ Appendix B. The measured ILS parameters of the two Harvard EM27/SUNs are also consistent over time and across continent, as given in Appendix A.

	$\overline{R_{CH_4}}$		$\overline{R_{CO_2}}$	
	GFIT	PROFFIT	GFIT	PROFFIT
Before	0.99574	0.99813	0.99877	0.99838
During	0.99580	0.99809	0.99881	0.99834
Both	0.99578	0.99810	0.99880	0.99835

Table 1. Calibration factors $\overline{R_G}$ for X_{CH_4} and X_{CO_2} before and during the field campaign, determined by forcing linear regression line go through zero. $\overline{R_G}$, determined using all data, are provided in the last row and used for the field study.

Figure 2. Scatter plots with the slopes representing $\overline{R_G}$ for different days using I2S/GFIT retrieval (top panels) and PROFFIT retrieval (bottom panels). January measurements are carried out in Pasadena, others in Boston. The first four days are before the field study, others are during the campaign.

4 Scientific Applications

4.1 Emission of an Area Source

We measured the column-averaged dry-air mole fractions X_{CO_2} and X_{CH_4} simultaneously at locations upwind and downwind of the dairy farms in Chino, California, for several days in January 2015. Field results are shown for *ha, hb*, and *pl* in Fig. 3.

5   Meteorological conditions were particularly favorable on 24 Jan. 2015, with consistent wind directions and wind speeds ($\sim$10 m ~~/s~~s^{-1}) at both Chino airport (KCNO: 1 km northeast of the downwind station ha) and Ontario airport (KONT: 3 km north of the upwind station hb) (see Fig. 3 (c) panels 3 and 4). 5 minutes averaged wind information from Automated Surface Observing System (ASOS) is used.

    The measured methane enhancement ΔX_{CH_4} was notably consistent at $\sim$2 ppb over 5 hours of measurement (Fig. 3 (c),

10 ~~Tab.~~Table 2), 10 times larger than our measurement precision using 5 min integration time (see Sec. 3.1). Times between 0.1 ~~-0.7~~ and 0.7 hours from solar noon were not taken into account, because ~~a transient peak was~~ transient peaks were measured at the upwind site. The transient peaks are also observable at the downwind site, but weaker due to dispersion. More discussion on the transient peaks can be found in Sec. 4.3.2.

    Winds were more variable on 15 Jan. 2015 (Appendix F), with a consistent period of just $\sim$1 hour with relatively light wind

15 ($\sim$2 m ~~/s~~s^{-1}) at the two airports. The observed ΔX_{CH_4} was $\sim$10 ppb (Fig. 3 (d)), a factor of 5 larger than on the 24th, showing inverse proportionality to the wind speed.

    We use a simple column model (Jacob (1999)) and literature emission values to *estimate* ΔX_G for the dairy farms (area source) and to *verify* our measurements:

$$\Delta X_G = X_G^d - X_G^u = \frac{D}{\overline{U}} \times \frac{E_G}{\text{column}_{\text{dryair}}}, \tag{2}$$

20   where ~~column$_{\text{dryair}}$ denotes the column number density of dry air.~~ E_G is the mean emission flux ~~[molec./(m^{2}s)]~~ (unit: molec. m^{-2} s^{-1}) along the line traversing the area source along the direction sampled at the downwind station, and D is the length of the transect. column$_{\text{dryair}}$ denotes the mean column number density of dry air. The frame of reference is the air column, which picks up the emissions of gas G from the dairies as the air traverses the farms. The longer the air column travels in the emission field, the larger the difference between the column number densities of the downwind and upwind sites will become.

25 ΔX_G is therefore proportional to the residence time $D/\overline{U}$ of the air column, and inversely proportional to the wind speed $\overline{U}$. This simple column model is applicable when the wind direction and speed are consistent across the area, and fluxes are uniform at plume scale.

    Our model assumes that air parcels within the air column are transported with a mean velocity $\overline{U}$ in the horizontal direction, which can be estimated using real-time data for the wind speed at the surface. Using Reynolds' decomposition, the time series
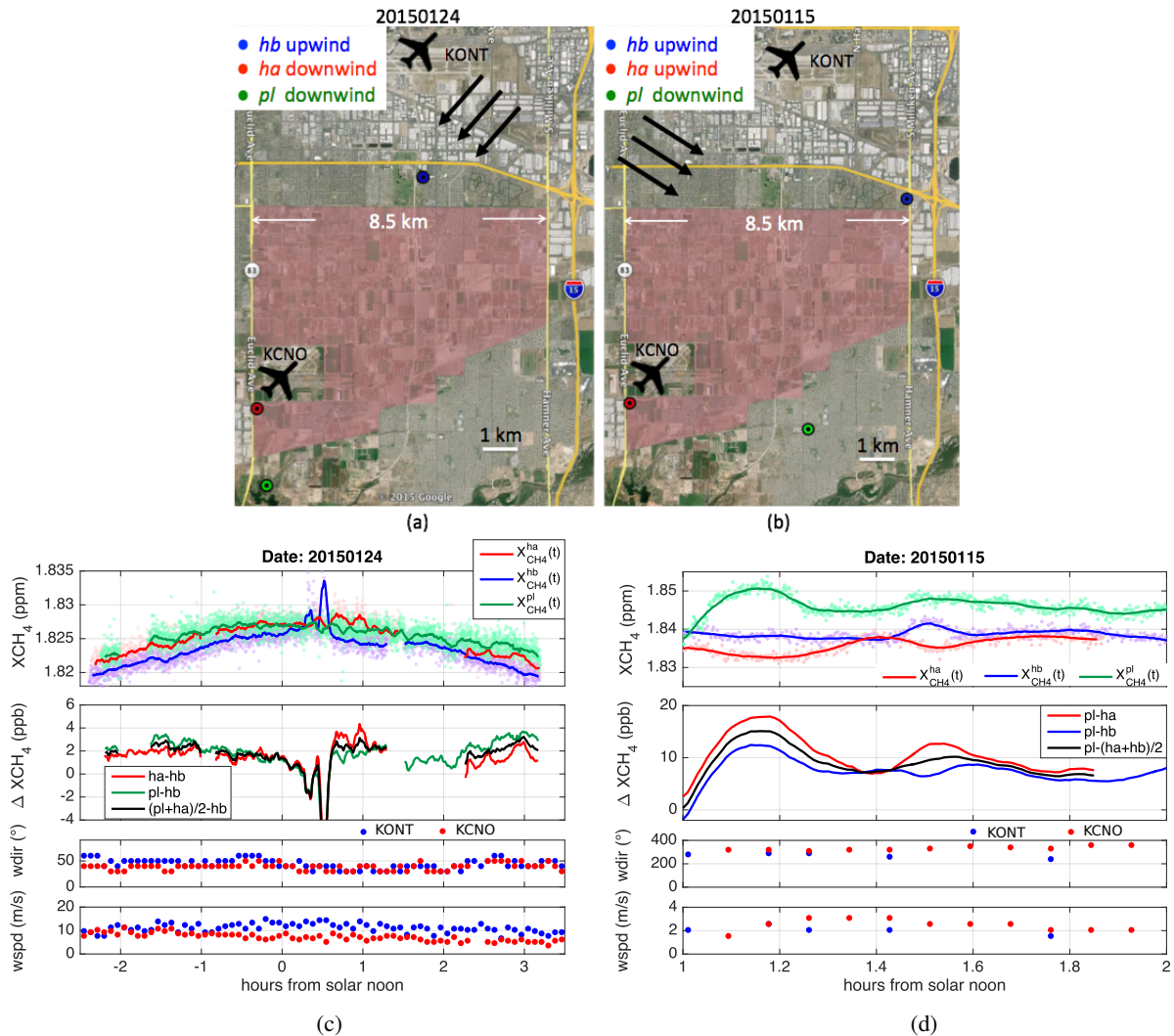
Figure 3. (a) and (b): locations of FTS stations and mean wind directions on 15 and 24 Jan., 2015. (c) and (d): column-averaged DMF measurements at three stations and downwind minus upwind differences (solar zenigh angle $\leq 70°$). On 24 Jan., ΔX_{CH_4} was steady at ~ 2 ppb most of the day, 10 times larger than our measurement precision; on 15 Jan., $\Delta X_{CH_4}(t)$ was ~ 10 ppb, about 5 times larger than on 24 Jan., showing inverse proportionality to the wind speed. Map provided by Google Earth, Image Landsat, Data SIO, NOAA, U.S. Navy, NGA, and GEBCO.

of horizontal (u) and vertical (w) wind speed are split into a mean part and a turbulent part, i.e.:

$$u(t) = \overline{u} + u_{\text{turb}}(t), \qquad\qquad\qquad w(t) = \overline{w} + w_{\text{turb}}(t), \tag{3}$$

$$\sigma_u = \sqrt{<u_{\text{turb}}^2>}, \qquad\qquad\qquad \sigma_w = \sqrt{<w_{\text{turb}}^2>}. \tag{4}$$

σ_u and σ_w are the standard deviations of the turbulent components. We assume the turbulence is horizontally homogeneous
5   (σ_u is independent of location) and isotropic ($\sigma_w = \sigma_u$), and that the mean vertical wind speed $\overline{w}$ is zero. Strictly speaking, $\overline{U}$
denotes the *mass-enhancement-weighted* wind velocity, i.e. $\overline{u}(z)$ weighted with the vertical distribution of the CH_4 molecules
emitted from the dairies, denoted as $\text{PDF}_{\Delta CH_4}(z)$, i.e.

$$\overline{U} = \int_0^\infty \overline{u}(z)\,\text{PDF}_{\Delta CH_4}(z)dz. \tag{5}$$

Note if $\overline{u}(z) = \text{const.}$, we have $\overline{U} = \overline{u}(z) = \text{const.}$, i.e. $\overline{U}$ is independent of the vertical distribution of the CH_4 molecules being
10   added in the column. However, since the wind speed generally increases with altitude, $\text{PDF}_{\Delta CH_4}(z)$ needs to be considered for
the estimate of $\overline{U}$.

We assume ΔCH_4 is uniformly distributed up to a mixing height z_{emiss} and negligible above, then:

$$\text{PDF}_{\Delta CH_4}(z) = \begin{cases} \frac{1}{z_{\text{emiss}}}, & 0 \leq z \leq z_{\text{emiss}}, \\ 0, & z > z_{\text{emiss}}, \end{cases} \tag{6}$$

$$\overline{U} = \frac{1}{z_{\text{emiss}}} \int_0^{z_{\text{emiss}}} \overline{u}(z)dz. \tag{7}$$

15   We use a 2D random walk model (McCrea and Whipple (1940)) to estimate z_{emiss}, the height to which CH_4 emissions are
transported vertically by turbulent flow. The number of the random-walk steps n is given by the ratio between the average
transit time of the emission τ_{transit} and the decorrelation time of the turbulent velocities τ_{eddy}, i.e.,

$$n = \frac{\tau_{\text{transit}}}{\tau_{\text{eddy}}} = \frac{D\sigma_w}{2\overline{u}\lambda}. \tag{8}$$

Assuming homogeneous emission, τ_{transit} is approximately $D/2\overline{u}$, with $\overline{u}$ representing the mean speed at the surface. This also
20   corresponds to the transit time of a particle emitted at the center of the field. τ_{eddy} is given by λ/σ_w, where λ denotes the
average eddy scale.

On 24 Jan., the mean horizontal wind speed over the entire measurement time is 11.35 m s^{-1} at KONT and 7.29 m s^{-1}
at KCNO with standard deviations of 1.75 m s^{-1} and 1.59 m s^{-1}, respectively. The wind directions are likewise very
consistent over time, with a standard deviation of 8.9° (KONT) and 6.5° (KCNO). The wind speed at 10 m above ground
25   level (agl) is assumed to be the average at the two airports over time, which gives $\overline{u}(10\text{ m}) = 9.3$ m s^{-1} with fluctuations
$\sigma_u(10\text{ m}) = \sigma_w(10\text{ m}) = 1.7$ m s^{-1}. Assuming an average eddy scale of 100 m, the expected value of the height to which

CH_4 emissions rise is therefore:

$$z_{\text{emiss}} = \frac{\lambda \sqrt{n}}{\sqrt{2}} = \frac{1}{2} \sqrt{\frac{D \sigma_w (10\,\text{m}) \lambda}{\overline{u}(10\,\text{m})}} = \frac{1}{2} \sqrt{D\,I\,\lambda} \approx 200\,\text{m}. \tag{9}$$

According to Taylor's hypothesis (Taylor (1938)), the turbulence intensity $I = \sigma_u / \overline{u}$ should be constant, which indicates z_{emiss} does not depend on $\overline{u}$, but only on the eddy scale λ and the turbulence intensity.

5   For determining $\overline{U}$ we need to consider the wind profile both in and above the surface layer. The wind follows a roughly logarithmic profile in the surface layer. At the middle portion of the PBL, the wind has typically constant direction and speed (Stull (1988)). Because the surface roughness information is not available, we use the power law to approximate the log wind profile in the surface layer and assume a constant horizontal wind speed above, i.e.,

$$\overline{u}(z) = \begin{cases} \overline{u}(10\,\text{m}) \left(\frac{z}{10\,\text{m}}\right)^{\alpha}, & 0 \leq z \leq z_{\text{S}}, \\ \overline{u}(10\,\text{m}) \left(\frac{z_{\text{S}}}{10\,\text{m}}\right)^{\alpha}, & z_{\text{S}} < z < z_{\text{PBL}}, \end{cases} \tag{10}$$

10   where z_{S} and z_{PBL} denote the depth of the surface layer and the PBL, respectively. The power law exponent α is approximately $1/7$ for neutral stability conditions (Hsu et al. (1994)).

~~This wind model (Eq. 10) is consistent with the winds reported by aircraft taking off and landing at Ontario airport (see Appendix E).~~

Inserting Eq. 10 into Eq. 7, we obtain:

15
$$\overline{U} = \frac{\overline{u}(10\,\text{m})}{z_{\text{emiss}}} \left(\int_0^{z_{\text{S}}} \left(\frac{z}{10\,\text{m}}\right)^{\alpha} dz + \int_{z_{\text{S}}}^{z_{\text{emiss}}} \left(\frac{z_{\text{S}}}{10\,\text{m}}\right)^{\alpha} dz \right)$$
$$= \overline{u}(10\,\text{m}) \left(\frac{z_{\text{S}}}{10\,\text{m}}\right)^{\alpha} \left(1 - \frac{z_{\text{S}}}{z_{\text{emiss}}} \frac{\alpha}{\alpha + 1} \right). \tag{11}$$

Varying z_{S} in the range of 10 m to z_{emiss}, we obtain $\overline{U}$ in the range of 9.3 to 12.5 m ~~/s, or~~ $\underline{\text{s}^{-1}}$, corresponding to an average of 10.9 m ~~/s~~$\underline{\text{s}^{-1}}$ $\pm 15\%$. The lower bound is given by a constant wind speed starting from 10 m agl, and the upper bound assumes a wind profile power law up to the mixing height z_{emiss}.

20   Our wind model is consistent with the automated aircraft reports on profiles measured when taking off and landing at Ontario airport (ACARS profiles), and also agrees well with the Hybrid Single-Particle Lagrangian Integrated Trajectory model (HYSPLIT) simulations (Stein et al. (2015); Draxler and Hess (1998)), driven by the meteorological model "North American Mesoscale Forecast System (NAM)" with a horizontal resolution of 12 km. The comparison can be found in Appendix E.

     Oxygen column number density is determined as $4.493 \cdot 10^{28}$ molec. $\text{m}^{-2} \pm 0.5\%$ (Appendix D), accounting for 20.95% of 25 dry air. According to Eq. 2, the uncertainty in calculating E_{G} from ΔX_{G} is the sum of the uncertainties in $\overline{U}$ (15%), ΔX_G (~~0.1‰ precision~~$\underline{0.01\%\ \text{precision}}$), and column$_{\text{dryair}}$ (~~1~~$\underline{0.5}\%$)~~. Oxygen column number density is determined as $4.493 \cdot 10^{28}$ molec./m$^2 \pm 1\%$ (Fig.11), accounting for 20.95% of dry air~~, in total roughly 16%. Therefore, an emission estimate using differential column measurements is dominated by the uncertainty in the transport (i.e. $\overline{U}$), not the differential column measurements ~~themself~~themselves.

Since the two spectrometers have identical optical setup, spectral resolution, and measuring geometry, their column averaging kernels are very similar, and happen to be close to one at all altitudes (Hedelius et al. (2016)). The uncertainty arising from the differences in averaging kernels is included in the uncertainty in ΔX_G. The sensitivity of X_{CH_4} on surface pressure inputs ~~are~~ is discussed in Appendix C.

5   In ~~Tab.~~Table 2, the time-averaged ΔX_{CH_4} and their corresponding emission numbers are listed. Measurements between 0.1 and 0.7 hours after solar noon are neglected due to a transient peak measured with hb (Fig. 3).

Configuration	ΔX_{CH_4} (ppb)	E_{CH_4} ~~[molec./(m²s)]~~ [molec. m^{-2} s^{-1})]	$E_{CH_4,\text{annual}}$ ~~[Gg/yr]~~ [Gg yr^{-1}]
ha - hb	1.8	$5.38 \cdot 10^{17} (\pm 16\%)$	$22.5 (\pm 26\%)$
pl - hb	2.1	$6.14 \cdot 10^{17} (\pm 16\%)$	$25.7 (\pm 26\%)$
$(pl + ha)/2$ - hb	2.1	$6.09 \cdot 10^{17} (\pm 16\%)$	$25.5 (\pm 26\%)$
Peischl's bottom-up	$2.3 (\pm 0.6)$		28.0
Peischl's top-down	$(4.0 \pm 1.0) (\pm 50\%)$		$49.0 (\pm 50\%)$

Table 2. Time-averaged ΔX_{CH_4} ~~for~~, using ha or pl, or ha and pl as downwind stations on 24 Jan. 2015, and their corresponding emission numbers calculated using Eq. 2. ΔX_{CH_4} is rounded to one decimal place in the table, whereas for the calculation of E_{CH_4} and $E_{CH_4,\text{annual}}$ ~~are done with full~~ all available digits are used. 16% ~~is given by~~ follows from the uncertainties in $\overline{U}$, column$_{\text{dryair}}$, and ΔX_G. Uncertainty in $E_{CH_4,\text{annual}}$ is 16% added with 10% uncertainty in the emission area. This table also displays the annual emission rates estimated by Peischl et al. (2013) using bottom-up and top-down methods. The corresponding column differences ΔX_{CH_4} and their uncertainties, as derived in Eq. 12, are summarized in the second column.

We can compare our measurements to the value of ΔX_{CH_4} derived from literature annual mass emission rates $E_{CH_4,\text{annual}}$ for the dairy farms. Peischl et al. (2013) determined 28 Gg ~~/yr~~yr^{-1} using bottom-up method accounting for enteric fermentation and dry manure management, and $49(\pm 50\%)$ Gg ~~/yr~~yr^{-1} using top-down method ~~based on aircraft measurements~~ with
10   aircraft-based mass balance approach during the CalNex field study. We assume a dairy area (area$_{\text{emiss}}$) of 50 km$^2 \pm 10\%$ and a constant emission rate across the farm throughout day and night, to convert ~~$E_{CH_4,\text{annual}}$[g/yr] to E_{CH_4}[molec./(m²s)]~~ $E_{CH_4,\text{annual}}$[Gg yr^{-1}] to E_{CH_4}[molec. m^{-2} s^{-1})]. The transect length D is approximated with 8 km, which is the diameter of a circle with 50 km^2 area.

For 24 Jan. 2015,

$$15 \quad \Delta X_{CH_4,\text{Exp}} = \frac{D}{\overline{U}} \times \frac{E_{CH_4,\text{annual}}(\text{Peischl's Number})}{m_{CH_4} \cdot \text{area}_{\text{emiss}} \cdot N_{\text{s/year}} \cdot \text{column}_{\text{dryair}}}$$

$$= \begin{cases} 2.3 \pm 0.6 \text{ ppb}, & \text{for } 28 \text{ Gg yr}^{-1} \text{ (bottom-up estimate)}, \\ (4.0 \pm 1.0)(\pm 50\%) \text{ ppb}, & \text{for } 49(\pm 50\%) \text{ Gg yr}^{-1} \text{ (top-down estimate)}, \end{cases} \quad (12)$$

where m_{CH_4} denotes the molecular mass of methane [g/molec.] and $N_{\text{s/year}}$ represents the number of seconds per year.

The observed ΔX_{CH_4}, ~ 2 ppb (Fig. 3(c), ~~Tab.~~ Table 2), falls in the lower half of the range from Peischl. Our results, and Peischl's top-down estimates, both represent just a few days of data. The difference with Peischl's results using ~~aircraft measurements~~ the aircraft-based mass balance approach could be due to seasonal factors, activity levels at the farms, uncertainties in $\overline{U}$, as well as in background concentration and boundary layer height for the aircraft measurements (Cambaliza et al. (2014)), or model errors. Longer deployments with more ancillary data, such as wind profiles, would be needed to refine the result. Further studies using a WRF-LES model will be presented in Viatte et al. (2016). The differential column measurement using compact FTSs has shown the capability to determine the emission flux when deployed across an area source such as Chino farms.

4.2 Source Characterization Using Ratios of ~~Spatial~~ Column ~~Gradients~~ Differences

Pasadena is a city within the SCB with heterogeneous CO_2 and CH_4 emissions, from different source types such as transportation, electricity generation, industry, landfills, and gas leaks from natural gas delivery system. The ratio of column ~~gradients~~ differences can be used to characterize regional ~~emission ratios~~ emissions. For example, Wunch et al. (2009) measured diurnal changes of X_{CH_4}, X_{CO_2}, and X_{CO} (temporal ~~gradient~~ difference), and used the CO_2 emission inventories from the California Air Resources Board (CARB) and EDGAR (Emission Database for Global Atmospheric Research) to estimate emissions of CH_4 and CO in the South Coast air basin (SCB).

~~Pasadena is a city within the SCB with heterogeneous CO_2 and CH_4 emissions, from different source types such as transportation, electricity generation, industry, landfills, and gas leaks from natural gas delivery system. The two spectrometers~~ We deployed two EM27/SUN spectrometers, ha and hb ~~were~~, located north (34.2N, 118.13W, 557 m asl) and south (34.11N, 118.14W, 172 m asl) of Pasadena, on 27 Jan. 2015. ~~The spatial gradient at time t is given by the difference between the measurements of~~ We measured the column difference between ha and hb ~~at the same time~~ during the course of day, i.e. $\Delta X_G(t) = X_G^{hb}(t) - X_G^{ha}(t)$, which is shown in Fig. 4 third panel.

We determine the ratio of *spatial* column ~~gradients~~ differences $\Delta X_{CH_4}/\Delta X_{CO_2}$ across Pasadena, by linear regression of ΔX_{CH_4} and ΔX_{CO_2} data using maximum likelihood estimation (York et al. (2004), see Fig. 5). The ~~determined gradient~~ derived ratio over the course of the day (7.4 $\pm$ 0.1 ppb/ppm) is similar to the emission ratios determined by comparing the daily variations of X_{CH_4} and X_{CO_2} (7.8 $\pm$ 0.8 ppb/ppm) reported at a TCCON station (Wunch et al. (2009)) located at JPL (34.2N, 118.2W, 390 m asl), and likewise for the ratio of enhancements obtained by the CLARS-FTS (7.28 $\pm$ 0.09 ppb/ppm, Wong et al. (2015)), which compared DMFs from diffuse solar reflectance off a spectralon plate at Mount Wilson (34.22N, 118.06W, 1670 m asl) with those from reflected sunlight from West Pasadena (34.17N, 118.17W).

By coloring the ~~gradient ratios~~ ratios of column differences per hour (Fig. 6), we observe a difference in the ~~gradient~~ ratios between noon (9.8 $\pm$ 0.2 ppb/ppm) and afternoon time (6.8 $\pm$ 0.1 ppb/ppm), with both regression curves passing essentially through the origins. We determined a higher $\Delta X_{CO_2}/\Delta X_{CH_4}$ ratio in the afternoon than the noon time, which can be caused by more traffic emissions in the basin. The lagged cross covariance between ΔX_{CO_2} and ΔX_{CH_4} peaks at zero lag, and the peak value is interestingly higher than the peak value of the cross covariance function between X_{CO_2} and X_{CH_4} at individual sites
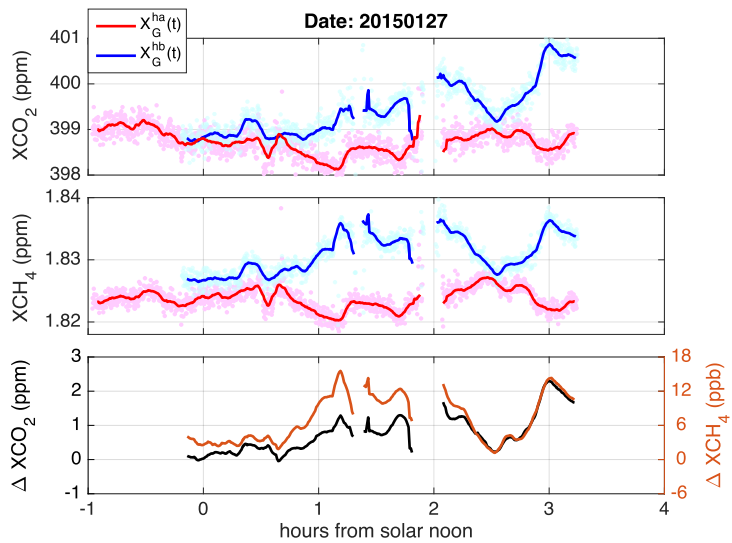
Figure 4. First and second panels: measured X_{CO_2} and X_{CH_4} north (ha) and south (hb) of Pasadena on 27 Jan. with 5 min averaging time. Third panel: ΔX_{CO_2} and ΔX_{CH_4} are temporal correlated and their ratio is determined as 7.4 ppb/ppm, shown in Fig. 5.
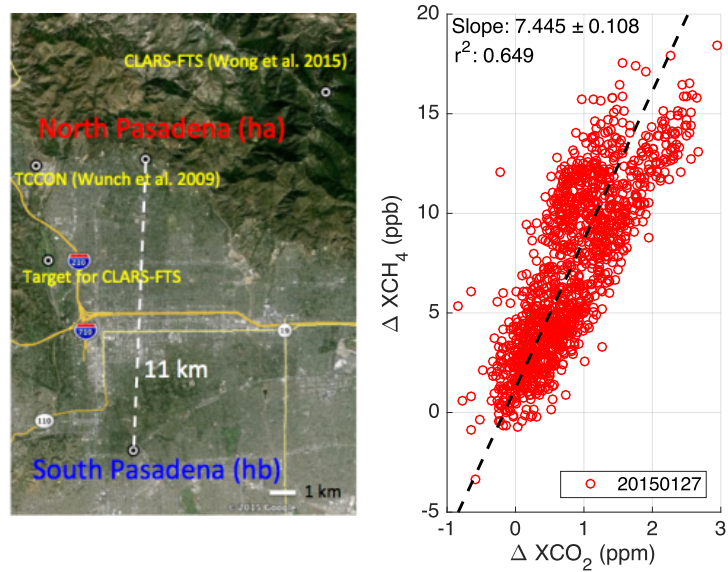
Figure 5. The derived ratio of column differences across Pasadena is similar to Wunch et al. (2009) using TCCON DMF daily dynamics and very close to the excess ratio determined in Wong et al. (2015), which compared DMFs from diffuse solar reflectance off a spectralon plate at Mount Wilson with those from reflected sunlight from West Pasadena. Map provided by Google Earth, Image Landsat, Data SIO, NOAA, U.S. Navy, NGA, and GEBCO.
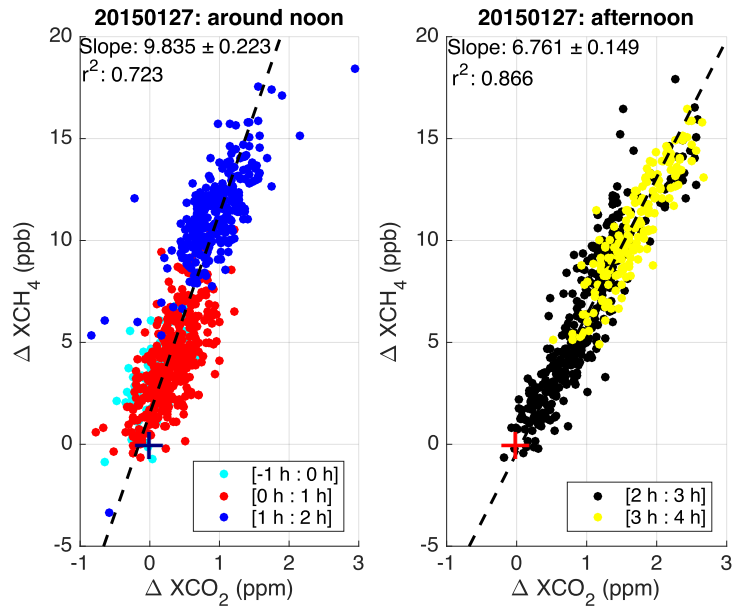
Figure 6. Column ~~gradient~~ difference ratio measured across Pasadena colored by hours. Left figure shows the time period between 1 hour before solar noon and 2 hours after solar noon, and right plot shows the time period 2 to 4 hours after solar soon. Both regression curves essentially pass through the origins that are shown as crosses.

(Fig. 15 in Appendix G), which suggests the ~~spatial gradient is also~~ column difference is sensitive to the emissions between the two sites.

The Pasadena study confirms that sources of CH_4 are surprisingly large from SCB, as reported by previous papers using aircraft and TCCON data (Wunch et al. (2009); Wennberg et al. (2012); Peischl et al. (2013)). The capability of ~~the column gradient ratio measurements for~~ determining emission ratios using ratios of spatial column differences is illustrated here.

4.3 Short-Term Variations

4.3.1 Side-by-side Measurements

We observed short-term variations in side by side measurements at Caltech and Harvard. These fluctuations are captured by both instruments simultaneously, representing geophysical phenomena, not noise as might be assumed. The high frequency temporal structure ($\sim$ 5-10 min Full Width at Half Maximum) can be caused by emissions not well mixed within the boundary layer ("plumes"), or by turbulence across the top of the ML, or by intrusions of a sea breeze front that introduces a different volume of air to the column, etc.

In Fig. 7 we show, as an example, side by side measurements at Caltech. Short-term variations in X_{CO_2} as large as 1 ppm are observed between 19:30 and 23:00 UTC. These features are only present in X_{CO_2}, not in X_{CH_4}, and are likely due to excess CO_2 emissions from a 12.5 MW natural gas power plant located $\sim$ 200 m to the south-southwest and/or a 0.1 MW solid
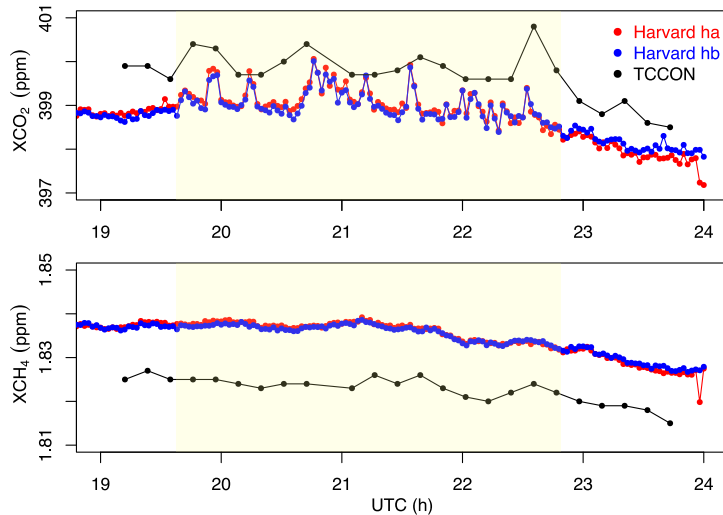
Figure 7. Side by side measurements on the roof of Caltech (17 Jan. 2015). Both EM27/SUN spectrometers (2 min block-average) captured short-term variations of X_{CO_2} signal (~ 1 ppm corresponds to ~~2.5‰~~ 0.25% relative). TCCON spectrometer does not resolve these short-term variation due to the low measurement rate.

oxide fuel cell ~ 20 m to the northwest. Note that, because the co-located TCCON spectrometer samples at a lower rate, these variations are not well resolved in the TCCON data (Wennberg et al. (2014)).

Fig. 8 shows another example in Boston where X_{CO_2} and X_{CH_4} vary together by approximately the same relative amount (~~1-2~~0.1-0.2%) at 12-13 UTC, also correlated with changes ($\sim 10\%$) in the mean relative backscatter (NRB) measured from our
5   LiDAR station 3 km away (Appendix H). The wind measurements at Boston Logan International Airport (KBOS), showing easterly winds during that time period, differ from New Bedford Regional Airport (KBED), indicating a sea breeze event that likely generates wind shear and turbulence across the top of the ML. The depth of PBL undergoes short-term variations that are also visible in the LiDAR data at 12:30 UTC. In this case, the column-averaged DMFs vary because the proportion of PBL air in the whole column changes. Also the sea breeze circulation pushes a different volume of air through the column, which could
10   result in a sporadic jump of X_{CO_2} and X_{CH_4}. The short-term variation of X_{CO_2} at ~~14-16~~14:30-15:30 UTC is not observed in X_{CH_4} and the LiDAR data. It is probably caused by CO_2 plumes within the PBL, similar to what we observed at Caltech and shown in Fig. 7.

4.3.2   Transient Peak at Chino

Not only for side-by-side measurements, but also in the field measurement, short term peaks are observed, as mentioned in
15   Sec.4.1. Transient peaks are moving from the upwind to the downwind site: they are observable at upwind site hb between 0.1 and 0.7 hours after solar noon, and at ha between 0.5 and 1.1 hours after solar noon (Fig. 9). They are not observable at pl site, probably because the plume is very narrow. Compared to the upwind peaks, the downwind peaks have a time shift, and
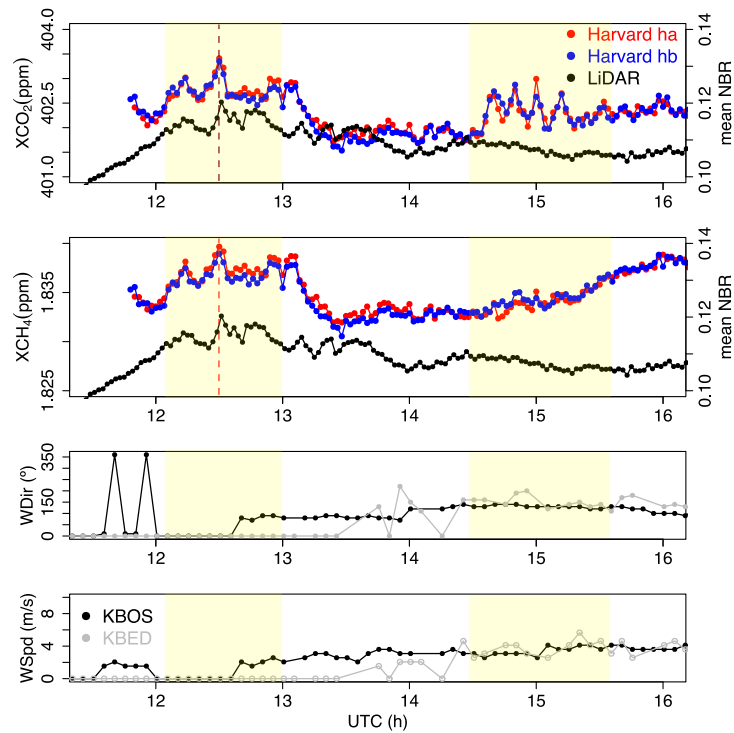
Figure 8. Short-term variations in X_{CO_2} and X_{CH_4} observed on the roof of Harvard Science Center by *ha* and *hb* (date: 16 April 2015; 2 min mean block average). A LiDAR metric of the thickness of the PBL (mean NRB 0-1.5 km agl) from a nearby site (Boston University, 3 km to the south-southeast of our site) is overlaid on top. The NRB signal is positively correlated with the short-term variations of the FTS measurements at 12-13 UTC.

are weaker and broader due to air dispersion. The peaks travelling from upwind to downwind site along the trajectory provide a proof that the same air mass is sampled.

The transient peaks are not observed in X_{CO_2}, indicating they are not caused by passing clouds, or from a powerplant. They may come from natural gas leaks from the pipelines in the Chino area, with some evidents being reported by environmental defense fund (EDF (2016)). The transient peaks are removed from the column difference study (Sec.4.1), because they are not associated with the local dairy farms.

The short-term variation helps us to understand the limitation of sampling using column measurements, which is relevant to the gradient determination and to satellite data. It is highly desirable to avoid aliasing these variations, and to characterize, model and/or measure the influences that cause these variations.
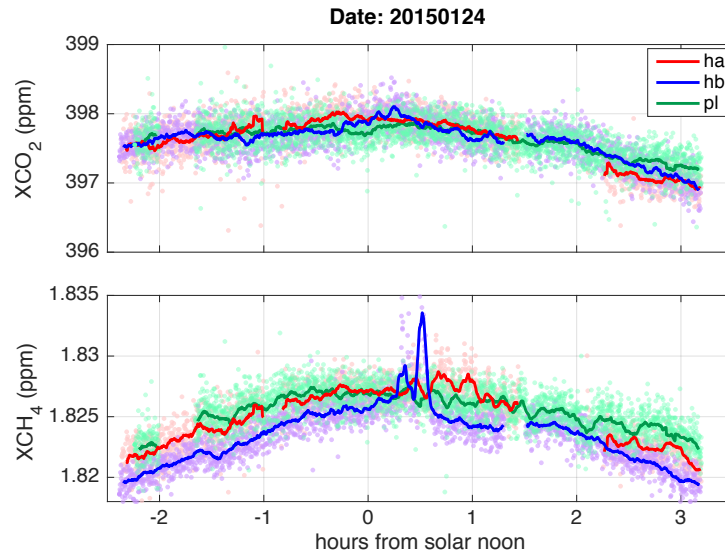
Figure 9. Observed column differences ΔX_{CO_2} (upper panel) and ΔX_{CH_4} (bottom panel) on 24 Jan. 2015, the transient peaks in X_{CH_4} are not observed for X_{CO_2}.

5 Conclusions

In this paper we demonstrated how to design observations of, and interpret, spatial gradients of column-averaged dry-air mole fractions for trace gases (CO_2, CH_4). We showed that the differential column methodology can be applied to the urban source problem and to other regional source-sink determinations.

We made extensive side-by-side measurements using two EM27/SUNs, in Boston and Pasadena, over many months. The differential system has a precision of ~~0.1‰~~ 0.01% for both X_{CO_2} and X_{CH_4} according to the Allan variance analysis when using an optimum integrating time of 10 min. The system is very stable in measuring column concentrations over time and after relocation across the continent.

We tested the gradient measurement and its sensitivity to emission sources, by measuring the ~~downwind minus upwind column gradient~~ downwind-minus-upwind column difference ΔX_{CH_4} across dairy farms in the Chino area. The signal-to-noise ratio for the ~~gradient~~ column difference determination was greater than 10, and the ~~observed column gradients~~ measured column gradient is inversely proportional to the wind speed. The derived emission numbers using a column model were consistent with ~~values derived from the emission numbers~~ the bottom-up source strength given by Peischl et al. (2013)~~. Spatial column gradient ratios~~, and lie on the lower end of their top-down estimates using aircraft-based mass balance approach. Ratios of spatial column differences $\Delta X_{CH_4}/\Delta X_{CO_2}$ were measured across Pasadena within South Coast air basin, with values consistent with emission ratios from the literature.

We observed significant short-term variations of X_{CH_4} and X_{CO_2}, and showed that they are not noise or variation of optical path length, but represent atmospheric phenomena. These measurements provide useful information for measuring pollution

plumes, ~~turbulences~~ turbulence across the top of the mixed layer~~and airmass variability within the PBL given by e.g. sea breeze circulation.~~, and transient peaks.

Overall, this paper helps to establish a range of new applications for compact solar-tracking Fourier transform spectrometers, and shows the capability of differential column measurements for determining urban emissions. By accurately measuring the

5   *differences* in the integrated column amounts across local and regional sources, we directly observe the mass loading of the atmosphere due to the influence of emissions in the intervening locale. The inference of the source strength is much more direct than inversion modeling using only surface concentrations, and less subject to errors associated with small-scale transport phenomena. The advent of compact, robust solar viewing spectrometers opens up myriad applications not hitherto pursued.

Appendix A: Instrument Line Function Parameters

10   The measured spectrum is a convolution between the atmospheric spectrum and instrument line shape in the frequency domain $ILS(\nu)$. In the ideal case, $ILS(\nu)$ is a delta function, which corresponds to a constant modulation efficiency for all optical path length differences. However, in practice, $ILS(\nu)$ is broader than a delta impulse, caused by the spectrometer's finite optical pathlength, finite aperture size and also misalignment of the interferometer. The ILS in the interferogram domain can be approximated using a simple model that assumes a linear decay of the modulation efficiency with increasing optical pathlength

15   difference and a constant phase error (Hase et al. (1999)).

We estimated the ILS parameters of both spectrometers with an experimental setup, similar as described in Frey et al. (2015) and determined the modulation efficiency at maximum optical path length (OPD_{max}) and phase error using the simple model implemented in the LINEFIT software (Hase et al. (1999)). Matlab scripts for automation purposes have been developed and can be obtained from the corresponding author.

20   Even though the measured ILS parameters are different for the two spectrometers due to the different internal alignment, the ILS of each single instrument is consistent over time and after relocation of the instrument across the contiguous US (see ~~Tab.~~ Table 3).

Boston		
Instrument	modulation efficiency at OPD_{max}	phase error (rad)
ha	0.975	$-3 \cdot 10^{-3}$
hb	0.988	$5 \cdot 10^{-3}$
Pasadena		
Instrument	modulation efficiency at OPD_{max}	phase error (rad)
ha	0.977	$-2 \cdot 10^{-3}$
hb	0.991	$4 \cdot 10^{-3}$

Table 3. Modulation efficiency and phase error determined for EM27/SUN ha and hb in Boston and Pasadena.

Instrument	$\overline{R_{\mathrm{CH_4}}}$	$\overline{R_{\mathrm{CO_2}}}$	$\overline{R_{\mathrm{O_2}}}$
ha	~~0.99577~~ 0.99578	0.99880	~~1.00848~~ 1.00846
pl	1.00093	0.99930	~~0.99713~~ 0.99712

Table 4. ~~Scaling~~ Calibration factors for ha and pl to match hb, for $X_{\mathrm{CH_4}}$, $X_{\mathrm{CO_2}}$ and ~~the~~ oxygen column number density measurements.

Appendix B: ~~Scaling~~ Calibration factors for ha and pl

~~Tab.~~ Table 4 shows the ~~scaling~~ calibration factors for ha and pl to match hb measurements, determined by linear regressions of the side-by-side measurements on the roof.

The linear models applied are:

$$X^{hb}_{\mathrm{CH_4}} = X^{ha}_{\mathrm{CH_4}} \cdot \overline{R^{ha}_{\mathrm{CH_4}}}, \qquad\qquad X^{hb}_{\mathrm{CH_4}} = X^{pl}_{\mathrm{CH_4}} \cdot \overline{R^{pl}_{\mathrm{CH_4}}}, \tag{B1}$$

$$X^{hb}_{\mathrm{CO_2}} = X^{ha}_{\mathrm{CO_2}} \cdot \overline{R^{ha}_{\mathrm{CO_2}}}, \qquad\qquad X^{hb}_{\mathrm{CO_2}} = X^{pl}_{\mathrm{CO_2}} \cdot \overline{R^{pl}_{\mathrm{CO_2}}}, \tag{B2}$$

$$\mathrm{column}^{hb}_{\mathrm{O_2}} = \mathrm{column}^{ha}_{\mathrm{O_2}} \cdot \overline{R^{ha}_{\mathrm{O_2}}}, \qquad\qquad \mathrm{column}^{hb}_{\mathrm{O_2}} = \mathrm{column}^{pl}_{\mathrm{O_2}} \cdot \overline{R^{pl}_{\mathrm{O_2}}}. \tag{B3}$$

Appendix C: Retrieval Sensitivity to Pressure Inputs ~~for 20150124 Retrievals~~

Surface pressure P_{surf} is a main input for the GFIT retrieval, to derive the site pressure altitude for each spectrum (Wunch et al. (2011)). Inaccurate pressure measurements will introduce errors in the computed widths of the gas absorption lines, i.e. pressure broadening, and therefore the fitted volume mixing ratio scale factors (Wunch et al. (2011)) will be inadequate, with a biased DMF as a result.

On 24 Jan., the surface pressure measurement at pl site failed, therefore we assess P^{pl}_{surf} using pressure measurements at the closest FTS station ha and the nearby airport KCNO. We assume hydrostatic equilibrium and a 1.18 hPa pressure difference per 10 m altitude difference. We derived ΔP_{surf} using the altitude difference between pl and ha, as well as pl and KCNO airport, and these two methods provide very similar results (Fig. 10). For the simple column model calculations, the retrieval with P^{pl}_{surf} computed using P^{ha}_{surf} and 1.652 hPa offset is used.

For consistency and a fair comparison with ha and pl, hb spectra are also retrieved with the surface pressure input calculated using P^{ha}_{surf} and a negative 7.788 hPa offset, given by 66 m altitude difference. The strong wind could affect the pressure measurement (Bernoulli's equation), which might be the reason for why hb retrieval using its on-site pressure measurements slightly diverges from the result using the pressure data derived from ha ~~met~~ weather station data (blue curve in Fig. 10).
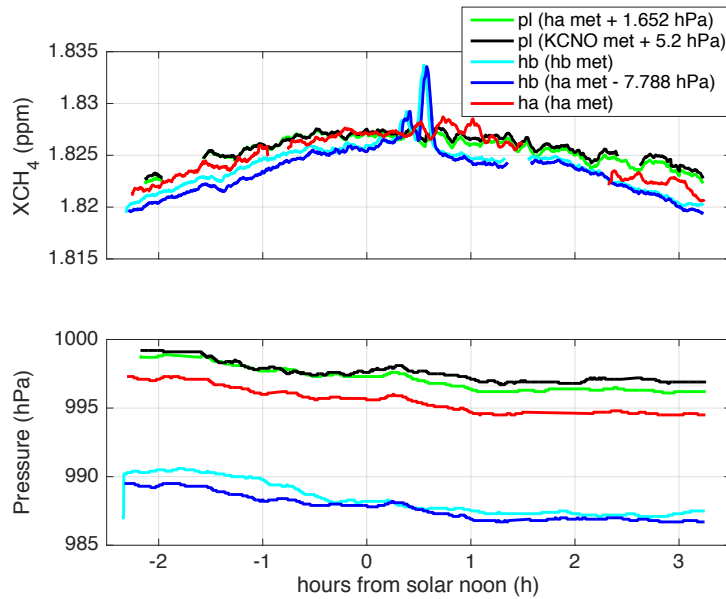
Figure 10. Surface pressure inputs (lower panel) and the corresponding X_{CH_4} retrieval results averaged for 5 min (upper panel). For Fig. 3(c) and the simple column model calculations, ha, hb and pl retrievals with the surface pressure inputs based on ha pressure measurements are used (red, blue and green curves).

Appendix D: ~~Oxygen~~ Dry Air Column Measurements on 24 Jan. 2015

Fig. 11 shows the ha, hb and pl measurements of oxygen column number densities. The deviations between three sites and the variations during the course of the day are given by the differences in atmospheric surface pressures and water column number densities. ha and pl measurements are scaled with the factors shown in ~~Tab.~~ Table 4 third column.

5   According to Fig.11, the oxygen column number density over the dairy area is $4.493 \cdot 10^{28}$ molec. m^{-2} $\pm 0.5\%$, which is used to calculate column$_{dryair}$, the column number density of dry air. column$_{dryair}$ is needed in the column model (Eq. 2) for the emission estimates. The uncertainty is mainly associated with the differences in altitudes between sites.

Appendix E: ~~ACARS aircraft profile data on 24 Jan. 2015~~Validation of Wind Model

As we have seen, the uncertainties in the wind speed estimates have a significant impact on the emission estimates. Hence, we
10   check our wind model for plausibility in the following, by comparing it with ACARS profiles and HYSPLIT simulations.

E1   ACARS Profile

In Fig. 12 we show the automated aircraft reports on profiles measured when taking off and landing at Ontario airport (MADIS ACARS profile data) and the automated surface observing system (ASOS) data, to examine the validity of the wind model

21
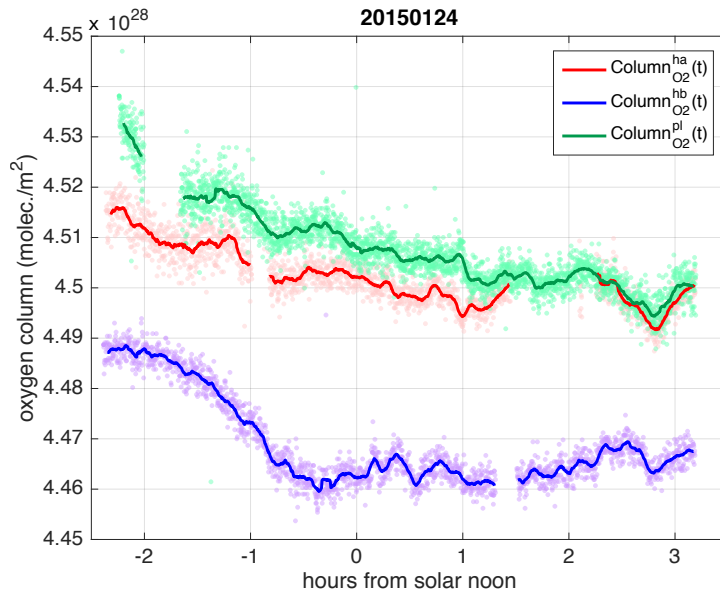
Figure 11. Oxygen column number densities measured by ha, hb and pl on 24 Jan. 2015.

described in Eq. 10. Two profiles were captured during the FTS measurement period, where only data above 2000 m agl are available, and two profiles after the measurement period. For plotting the model, we assume the surface layer height is $z_\text{S} = 100$ m and the power law exponent $\alpha = 1/7$.

The potential temperature profiles during the FTS measurements and 2-3 hours after are also shown in Fig. 12 third and
5   fourth panels. For the calculations we use the ACARS temperature profiles and the pressure profiles derived from the barometric formula, the ASOS sea level pressure data and a scale height of 7.4 km. Within the middle portion of the ML, the temperature profile follows adiabatic lapse rate, i.e. the potential temperature is nearly constant with height. This behavior is observed between roughly 200 m and 800 m agl at 2-3 hours after the measurement period. During the FTS measurement period, the airplanes capture data above 2100 m agl where the adiabatic process is not observed. Therefore the PBL height is determined
10   to be in the range of 800 to 2100 m agl. The surface layer is typically the bottom 10% of the PBL.

E2   HYSPLIT Simulation

We use the Hybrid Single-Particle Lagrangian Integrated Trajectory model (HYSPLIT) model to calculate the backward trajectories of tracers released from the FTS stations, starting at 20 UTC. We determine the wind speed from the travelled distance in one hour. To obtain a wind speed profile, multiple atitudes for the tracer release were chosen.
15   The simulated wind speeds are shown in Fig. 13. The blue curve represents the wind speed profile at the upwind site hb, and the red curve represents the wind speed profile at the downwind site ha. The black curve is the average of the two, which gives the mean wind profile.
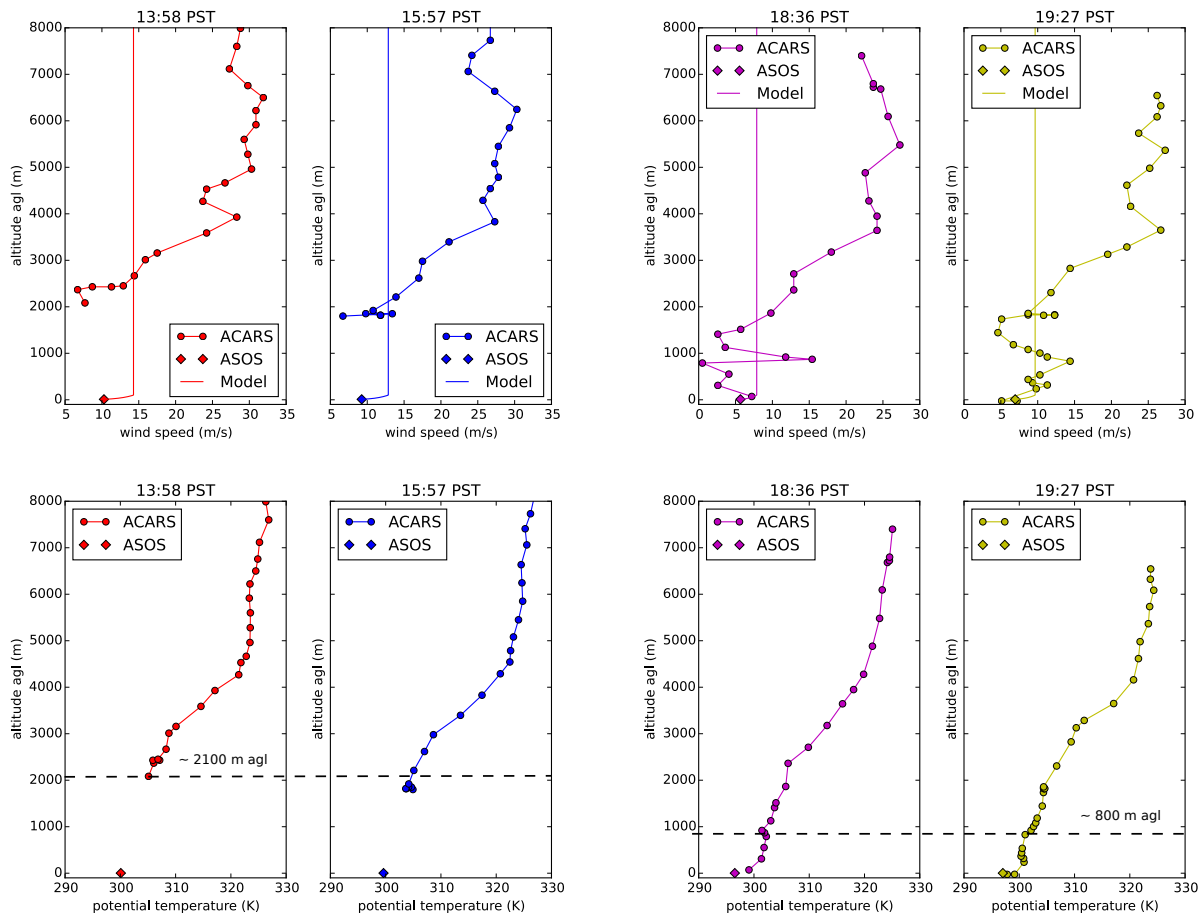
Figure 12. Vertical profile of the horizontal wind speed measurements and the calculated potential temperature profiles, at Ontario airport during (13:58 PST and 15:57 PST) and after the FTS measurements (18:36 PST and 19:27 PST).

In addition, the wind profile used in our emission estimate (Eq. 10) is illustrated in Fig. 13 with the grey lines. The lower bound is given by a constant wind speed starting from 10 m agl, and the upper bound assumes a wind profile power law up to the mixing height z_{emiss}, which is determined as around 200 m (Eq. 9) using a random walk model. The wind speed at 10 m agl is assumed as the average of KCNO and KONT airports between 19 and 20 UTC, which is identical to the wind speed at 10 agl determined using HYSPLIT.

In Fig. 13, the range given by our wind model covers the mean wind profile determined using the HYSPILT model (black curve). For the times between 19 and 20 UTC, $\overline{U}$ is determined as 11.6 m s^{-1} ± 15% using our wind model (Eq. 11), which is consistent with the value of 12.3 m s^{-1} obtained by averaging the HYSPILT wind profile vertically up to 200 m.

2015-01-24 19-20 UTC
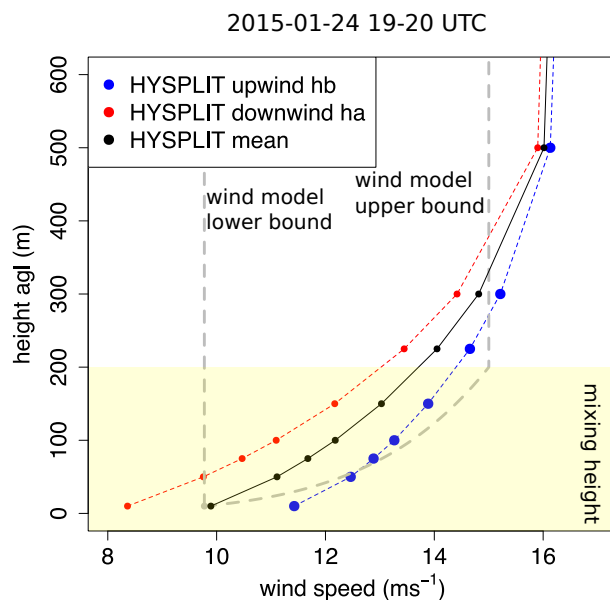
Figure 13. Comparison between our wind model and HYSPLIT simulations of wind speeds at different altitudes. The simulated mean wind profile (black curve) over Chino area is the averaged values of the profiles above the upwind site hb (blue curve) and the downwind site ha (red curve). The grey lines provide the range of our wind model.

## Appendix F: Column Difference Measurement on 15 Jan. 2015

Fig. 14 shows the measurements of X_{CH_4}, ΔX_{CH_4}, wind speeds, and wind directions for the entire day. For verifying the simple column model, we select the time period between 1 and 2 hours after solar noon with relatively consistent wind speeds and directions at KONT and KCNO. The data for the selected time window is shown in Fig. 3 (d).

Appendix G: Cross covariance function between the X_{CH_4} and X_{CO_2} on 27 Jan. 2015

The lagged cross covariance between X_{CH_4} and X_{CO_2} for individual sites measured with *ha* and *hb*, and between ΔX_{CH_4} and ΔX_{CO_2} are shown in Fig. 15.
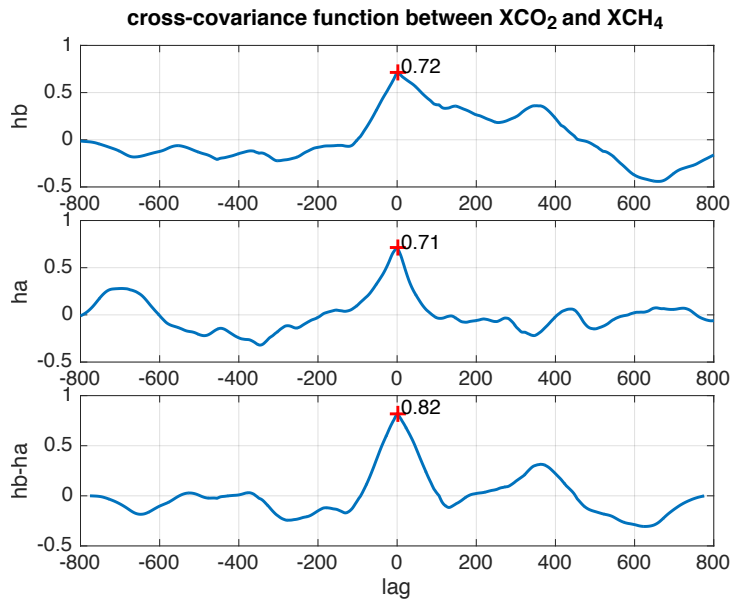
Appendix H: LiDAR measurement in Boston

Fig. 16 shows the normalized relative backscatter (NRB) signal recorded using a Mini Micro Pulse LiDAR (MiniMPL from company Sigma Space) on the roof of the Boston University (BU) on 16 April 2015. We integrate the NRB signal vertically from 0 to 1.5 km to obtain the mean NRB. The time series of the mean NRB together with our FTS measurements are shown in Fig. 8.

24
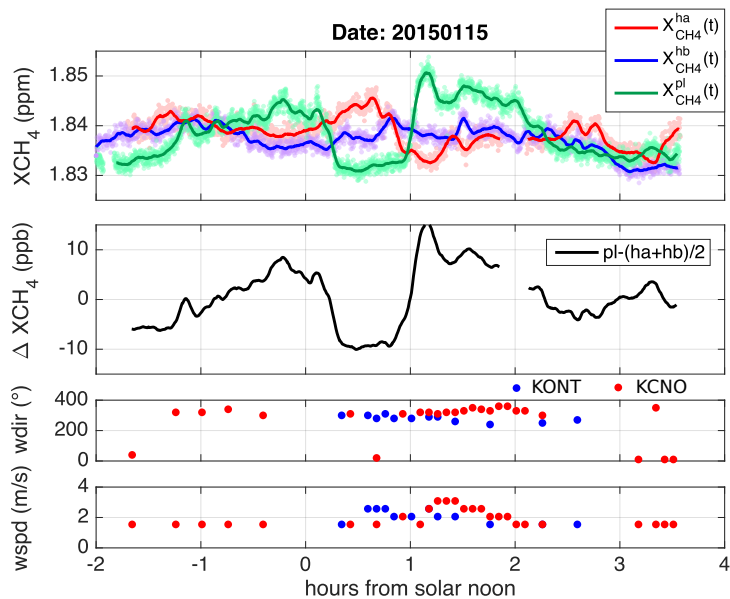
Figure 14. The whole day measurements on 15 Jan. 2015 for ha, hb and pl. We neglect the wind measurements with zero wind speed. Gradient measurements between 1 and 2 hours after solar noon are selected (Fig. 3 (d)) because of the relatively consistent wind speeds and directions at KONT and KCNO.

cross-covariance function between XCO$_2$ and XCH$_4$

Figure 15. The cross covariance function (mean-removed cross correlation) between X_{CH_4} and X_{CO_2} for individual sites measured with *ha* and *hb* are shown in first and second panels. The lagged cross covariance between ΔX_{CH_4} and ΔX_{CO_2} (third panel) has a larger value at zero lag compared to the first and second panels.

References

Allan, D. W.: Statistics of atomic frequency standards, Proceedings of the IEEE, 54, 221–230, 1966.

Bréon, F., Broquet, G., Puygrenier, V., Chevallier, F., Xueref-Remy, I., Ramonet, M., Dieudonné, E., Lopez, M., Schmidt, M., Perrussel, O., et al.: An attempt at estimating Paris area CO$_2$ emissions from atmospheric concentration measurements, Atmospheric Chemistry and

5   Physics, 15, 1707–1724, 2015.

Bruker: IFS 125HR User Manual, BRUKER OPTIK GmbH, 1st edn., 2006.

Cambaliza, M., Shepson, P., Caulton, D., Stirm, B., Samarov, D., Gurney, K. R., Turnbull, J., Davis, K., Possolo, A., Karion, A., et al.: Assessment of uncertainties of an aircraft-based mass balance approach for quantifying urban greenhouse gas emissions, Atmospheric Chemistry and Physics, 14, 9029–9050, 2014.

10   Chang, R. Y.-W., Miller, C. E., Dinardo, S. J., Karion, A., Sweeney, C., Daube, B. C., Henderson, J. M., Mountain, M. E., Eluszkiewicz, J., Miller, J. B., et al.: Methane emissions from Alaska in 2012 from CARVE airborne observations, Proceedings of the National Academy of Sciences, 111, 16 694–16 699, 2014.

Crisp, D., Miller, C. E., and DeCola, P. L.: NASA Orbiting Carbon Observatory: measuring the column averaged carbon dioxide mole fraction from space, Journal of Applied Remote Sensing, 2, 023 508–023 508, 2008.

15   Davis, S. P., Abrams, M. C., and Brault, J. W.: Fourier transform spectrometry, Academic Press, 2001.

Draxler, R. R. and Hess, G.: An overview of the HYSPLIT_4 modelling system for trajectories, Australian meteorological magazine, 47, 295–308, 1998.

EDF: Natural gas: Local leaks impact global climate, https://www.edf.org/climate/methanemaps, last visited 22 May 2016, 2016.
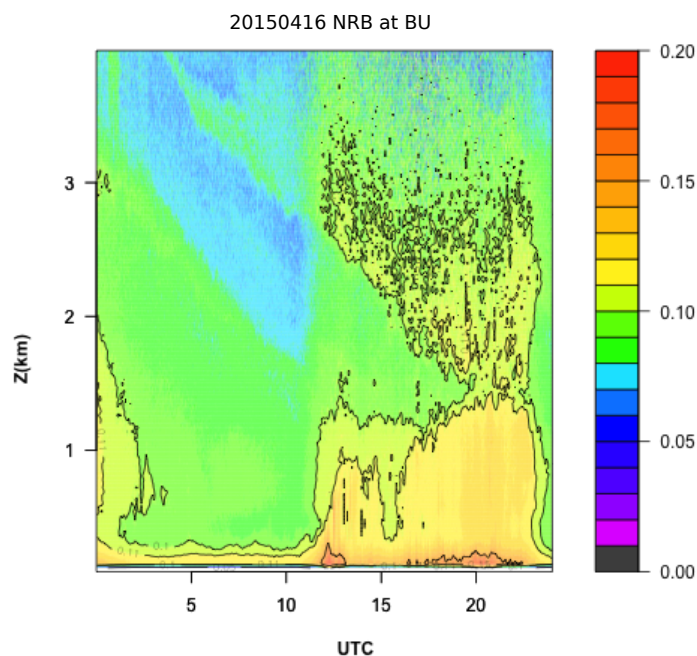
Figure 16. LiDAR measurement on the roof of Boston University on 20150416.

Frankenberg, C., Pollock, R., Lee, R., Rosenberg, R., Blavier, J.-F., Crisp, D., O'Dell, C., Osterman, G., Roehl, C., Wennberg, P., et al.: The Orbiting Carbon Observatory (OCO-2): spectrometer performance evaluation using pre-launch direct sun measurements., Atmospheric Measurement Techniques, 8, 2015.

Frey, M., Hase, F., Blumenstock, T., Groß, J., Kiel, M., Mengistu Tsidu, G., Schäfer, K., Sha, M., and Orphal, J.: Calibration and instrumental
5   line shape characterization of a set of portable FTIR spectrometers for detecting greenhouse gas emissions, Atmospheric Measurement Techniques, 8, 3047–3057, 2015.

Fu, D., Pongetti, T., Blavier, J.-F., Crawford, T., Manatt, K., Toon, G., Wong, K., and Sander, S.: Near-infrared remote sensing of Los Angeles trace gas distributions from a mountaintop site, Atmospheric Measurement Techniques, 7, 713–729, 2014.

Gisi, M., Hase, F., Dohe, S., and Blumenstock, T.: Camtracker: a new camera controlled high precision solar tracker system for FTIR-
10   spectrometers, Atmospheric Measurement Techniques, 4, 47–54, doi:10.5194/amt-4-47-2011, 2011.

Gisi, M., Hase, F., Dohe, S., Blumenstock, T., Simon, A., and Keens, A.: XCO_2-measurements with a tabletop FTS using solar absorption spectroscopy, Atmospheric Measurement Techniques, 5, 2969–2980, 2012.

Griffiths, P. R. and De Haseth, J. A.: Fourier transform infrared spectrometry, vol. 171, John Wiley & Sons, 2007.

Grimm, N. B., Faeth, S. H., Golubiewski, N. E., Redman, C. L., Wu, J., Bai, X., and Briggs, J. M.: Global change and the ecology of cities,
15   science, 319, 756–760, 2008.

Gurney, K. R., Romero-Lankao, P., Seto, K. C., Hutyra, L. R., Duren, R., Kennedy, C., Grimm, N. B., Ehleringer, J. R., Marcotullio, P., Hughes, S., et al.: Climate change: Track urban emissions on a human scale, Nature, 525, 179–181, 2015.

Hannigan, J. W.: NDACC IRWG: Evolution of Ground-Based Global Trace Gas Infrared Remote Sensing, in: Fourier Transform Spectroscopy, p. FMC1, Optical Society of America, 2011.

Hase, F., Blumenstock, T., and Paton-Walsh, C.: Analysis of the instrumental line shape of high-resolution Fourier transform IR spectrometers with gas cell measurements and new retrieval software, Applied Optics, 38, 1999.

5   Hase, F., Hannigan, J., Coffey, M., Goldman, A., Höpfner, M., Jones, N., Rinsland, C., and Wood, S.: Intercomparison of retrieval codes used for the analysis of high-resolution, ground-based FTIR measurements, Journal of Quantitative Spectroscopy and Radiative Transfer, 87, 25–52, 2004.

Hase, F., Frey, M., Blumenstock, T., Groß, J., Kiel, M., Kohlhepp, R., Mengistu Tsidu, G., Schäfer, K., Sha, M., and Orphal, J.: Application of portable FTIR spectrometers for detecting greenhouse gas emissions of the major city Berlin, Atmospheric Measurement Techniques,
10   8, 3059–3068, 2015.

Hedelius, J. K., Viatte, C., Wunch, D., C., R., Toon, G. C., Chen, J., Jones, T., Wofsy, S. C., Franklin, J. E., Parker, H., Dubey, M., and Wennberg, P. O.: Assessment of errors and biases in Xgas retrieved from a low resolution spectrometer (EM27/SUN), submitted to Atmospheric Measurement Techniques, amt-2016-39, initial submission, 2016.

Hsu, S., Meindl, E. A., and Gilhousen, D. B.: Determining the power-law wind-profile exponent under near-neutral stability conditions at
15   sea, Journal of Applied Meteorology, 33, 757–765, 1994.

Jacob, D.: Introduction to atmospheric chemistry, Princeton University Press, 1999.

Klappenbach, F., Bertleff, M., Kostinek, J., Hase, F., Blumenstock, T., Agusti-Panareda, A., Razinger, M., and Butz, A.: Accurate mobile remote sensing of XCO 2 and XCH 4 latitudinal transects from aboard a research vessel, Atmospheric Measurement Techniques, 8, 5023–5038, 2015.

20   Kort, E. A., Frankenberg, C., Miller, C. E., and Oda, T.: Space-based observations of megacity carbon dioxide, Geophysical Research Letters, 39, 2012.

Kort, E. A., Frankenberg, C., Costigan, K. R., Lindenmaier, R., Dubey, M. K., and Wunch, D.: Four corners: The largest US methane anomaly viewed from space, Geophysical Research Letters, 41, 6898–6903, 2014.

Lindenmaier, R., Dubey, M. K., Henderson, B. G., Butterfield, Z. T., Herman, J. R., Rahn, T., and Lee, S.-H.: Multiscale observations of
25   CO_2, $^{13}CO_2$, and pollutants at Four Corners for emission verification and attribution, Proceedings of the National Academy of Sciences, 111, 8386–8391, 2014.

McCrea, W. and Whipple, F.: Random Paths in Two and Three Dimensions., Proceedings of the Royal Society of Edinburgh, 60, 281–298, 1940.

McKain, K., Wofsy, S. C., Nehrkorn, T., Eluszkiewicz, J., Ehleringer, J. R., and Stephens, B. B.: Assessment of ground-based atmospheric
30   observations for verification of greenhouse gas emissions from an urban region, Proceedings of the National Academy of Sciences, 109, 8423–8428, 2012.

Mellqvist, J., Samuelsson, J., Johansson, J., Rivera, C., Lefer, B., Alvarez, S., and Jolly, J.: Measurements of industrial emissions of alkenes in Texas using the solar occultation flux method, Journal of Geophysical Research: Atmospheres (1984–2012), 115, 2010.

Peischl, J., Ryerson, T. B., Brioude, J., Aikin, K. C., Andrews, A. E., Atlas, E., Blake, D., Daube, B. C., de Gouw, J. A., Dlugokencky, E.,
35   Frost, G. J., Gentner, D. R., Gilman, J. B., Goldstein, A. H., Harley, R. A., Holloway, J. S., Kofler, J., Kuster, W. C., Lang, P. M., Novelli, P. C., Santoni, G. W., Trainer, M., Wofsy, S. C., and Parrish, D. D.: Quantifying sources of methane using light alkanes in the Los Angeles basin, California, Journal of Geophysical Research: Atmospheres, 118, 4974–4990, 2013.

Picarro: Datasheet G2301 CRDS Analyzer for CO_2, CH_4, H_2O Measurements in Air, https://picarro.app.box.com/s/5er36ac0ncmy1eruxge1p231cy00sl7k, 2015a.

Picarro: Datasheet G2401 CRDS Analyzer for CO_2, CO, CH_4, H_2O in Air, https://picarro.app.box.com/s/vfh80atc42tnq04t4a996t8sestqov9x, 2015b.

5   Stein, A., Draxler, R., Rolph, G., Stunder, B., Cohen, M., and Ngan, F.: NOAA's HYSPLIT atmospheric transport and dispersion modeling system, Bulletin of the American Meteorological Society, 96, 2059–2077, 2015.

Stremme, W., Ortega, I., and Grutter, M.: Using ground-based solar and lunar infrared spectroscopy to study the diurnal trend of carbon monoxide in the Mexico City boundary layer, Atmospheric Chemistry and Physics, 9, 8061–8078, 2009.

Stremme, W., Grutter, M., Rivera, C., Bezanilla, A., Garcia, A., Ortega, I., George, M., Clerbaux, C., Coheur, P.-F., Hurtmans, D., et al.:
10   Top-down estimation of carbon monoxide emissions from the Mexico Megacity based on FTIR measurements from ground and space, Atmospheric Chemistry and Physics, 13, 1357–1376, 2013.

Stull, R. B.: An introduction to boundary layer meteorology, vol. 13, Springer Science & Business Media, 1988.

Taylor, G. I.: The spectrum of turbulence, in: Proceedings of the Royal Society of London A: Mathematical, Physical and Engineering Sciences, vol. 164, pp. 476–490, The Royal Society, 1938.

15   Té, Y., Dieudonné, E., Jeseck, P., Hase, F., Hadji-Lazaro, J., Clerbaux, C., Ravetta, F., Payan, S., Pépin, I., Hurtmans, D., et al.: Carbon monoxide urban emission monitoring: A ground-based FTIR case study, Journal of atmospheric and oceanic technology, 29, 911–921, 2012.

Toon, G., Blavier, J.-F., Washenfelder, R., Wunch, D., Keppel-Aleks, G., Wennberg, P., Connor, B., Sherlock, V., Griffith, D., Deutscher, N., et al.: Total column carbon observing network (TCCON), in: Fourier Transform Spectroscopy, p. JMA3, Optical Society of America,
20   2009.

UNHabitat: Global Report on Human Settlement 2011, http://mirror.unhabitat.org/downloads/docs/E_Hot_Cities.pdf, visited 12 Nov. 2015, 2011.

Veefkind, J., Aben, I., McMullan, K., Förster, H., De Vries, J., Otter, G., Claas, J., Eskes, H., De Haan, J., Kleipool, Q., et al.: TROPOMI on the ESA Sentinel-5 Precursor: A GMES mission for global observations of the atmospheric composition for climate, air quality and
25   ozone layer applications, Remote Sensing of Environment, 120, 70–83, 2012.

Viatte, C., Lauvaux, T., Hedelius, J. K., Parker, H., Chen, J., Jones, T., Franklin, J. E., Deng, A. J., Gaudet, B., Verhulst, K., Duren, R., Wunch, D., Roehl, C., Dubey, M. K., Wofsy, S. C., and Wennberg, P. O.: Methane emissions from dairies in the Los Angeles Basin, Atmospheric Chemistry and Physics, doi:10.5194/acp-2016-281, in review, 2016.

Wennberg, P. O., Mui, W., Wunch, D., Kort, E. A., Blake, D. R., Atlas, E. L., Santoni, G. W., Wofsy, S. C., Diskin, G. S., Jeong, S., et al.:
30   On the sources of methane to the Los Angeles atmosphere, Environmental science & technology, 46, 9282–9289, 2012.

Wennberg, P. O., Wunch, D., Roehl, C., Blavier, J.-F., Toon, G. C., and Allen, N.: TCCON data from California Institute of Technology, Pasadena, California, USA, Release GGG2014R1, TCCON data archive, hosted by the Carbon Dioxide Information Analysis Center, Oak Ridge National Laboratory, Oak Ridge, Tennessee, U.S.A., doi:10.14291/tccon.ggg2014.pasadena01.R1/1182415, 2014.

Werle, P., Mücke, R., and Slemr, F.: The limits of signal averaging in atmospheric trace-gas monitoring by tunable diode-laser absorption
35   spectroscopy (TDLAS), Applied Physics B, 57, 131–139, 1993.

WHO: http://www.who.int/gho/urban_health/situation_trends/urban_population_growth_text, visited on 28 Oct. 2015, 2014.

Wong, K., Fu, D., Pongetti, T., Newman, S., Kort, E., Duren, R., Hsu, Y.-K., Miller, C., Yung, Y., and Sander, S.: Mapping CH_4: CO_2 ratios in Los Angeles with CLARS-FTS from Mount Wilson, California, Atmospheric Chemistry and Physics, 15, 241–252, 2015.

Wunch, D., Wennberg, P. O., Toon, G. C., Keppel-Aleks, G., and Yavin, Y. G.: Emissions of greenhouse gases from a North American megacity, Geophysical Research Letters, 36, L15 810, 2009.

Wunch, D., Toon, G. C., Wennberg, P. O., Wofsy, S. C., Stephens, B. B., Fischer, M. L., Uchino, O., Abshire, J. B., Bernath, P., Biraud, S. C., et al.: Calibration of the Total Carbon Column Observing Network using aircraft profile data, Atmospheric Measurement Techniques, 3, 1351–1362, 2010.

Wunch, D., Toon, G. C., Blavier, J. F., Washenfelder, R. A., Notholt, J., Connor, B. J., Griffith, D. W., Sherlock, V., and Wennberg, P. O.: The total carbon column observing network, Philos Trans A Math Phys Eng Sci, 369, 2087–112, 2011.

Wunch, D., Toon, G. C., Sherlock, V., Deutscher, N. M., Liu, X., Feist, D. G., and Wennberg, P. O.: The Total Carbon Column Observing Network's GGG2014 Data Version, Carbon Dioxide Information Analysis Center, Oak Ridge National Laboratory, Oak Ridge, Tennessee, USA, 10, doi:10.14291/tccon.ggg2014.documentation.R0/1221662, 2015.

York, D., Evensen, N. M., Martınez, M. L., and Delgado, J. D. B.: Unified equations for the slope, intercept, and standard errors of the best straight line, American Journal of Physics, 72, 367–375, 2004.